Resilient Pathways to Atomic Attachment of Quantum Dot Dimers and Artificial Solids from Faceted CdSe Quantum Dot Building Blocks

Justin C. Ondry,[†] John P. Philbin,[†] Michael Lostica,[†] Eran Rabani,[†,‡,#] and A. Paul Alivisatos*[,†,‡,§,⊥]

[†]Department of Chemistry, University of California, Berkeley, California 94720, United States

[‡]Materials Sciences Division, Lawrence Berkeley National Laboratory, Berkeley, California 94720, United States

[#]The Sackler Center for Computational Molecular and Materials Science, Tel Aviv University, Tel Aviv 69978, Israel

[§]Department of Materials Science and Engineering, University of California, Berkeley, California 94720, United States

[⊥]Kavli Energy NanoScience Institute, Berkeley, California 94720, United States

Abstract

The goal of this work is to identify favored pathways for preparation of defect resilient attached wurtzite CdX (X = S, Se, Te) nanocrystals. We seek guidelines for oriented attachment of faceted nanocrystals that are most likely to yield pairs of nanocrystals with either few or no electronic defects, or electronic defects that are in and of themselves desirable and stable. Using a combination of *in-situ* high resolution transmission electron microscopy (HRTEM) and electronic structure calculations, we evaluate the relative merits of atomic attachment of wurtzite CdSe nanocrystals on the $\{1\bar{1}00\}$ or $\{11\bar{2}0\}$ family of facets. Pairwise attachment on either facet can lead to perfect interfaces, provided the nanocrystal facets are perfectly flat and the angles between the nanocrystals can adjust during the assembly. Considering defective attachment, we observe for $\{1\bar{1}00\}$ facet attachment that only one type of edge dislocation forms, creating deep hole traps. For $\{11\bar{2}0\}$ facet attachment, we observe that four distinct types of dislocations form, some of which lead to deep hole traps while others only to shallow hole traps. HRTEM movies of the dislocation dynamics show that dislocations at $\{1\bar{1}00\}$ interfaces can be removed, albeit slowly. Whereas only some extended dislocations at $\{11\bar{2}0\}$ interfaces could be removed, others were trapped at the interface. Based on these insights, we identify the most resilient pathways to atomic attachment of pairs of wurtzite CdX nanocrystals and consider how these insights can translate to creation of electronically useful materials from quantum dots with other crystal structures.

Keywords: nanocrystals, oriented attachment, dislocations, CdSe, electronic structure, in situ TEM

Self-assembly of colloidal nanocrystals (NCs) into superlattices is a tunable strategy with great potential to prepare materials with rationally designed properties.[1] Much of the tunability comes from the separation of the synthesis of individual NC building blocks from the assembly process.

The ability to systematically control factors such as NC size,[2] surface ligands,[3–6] assembly solvent,[5] NC faceting,[7] assembly method,[8–11] and other factors have allowed the preparation of superlattices with impressive 2D[12] and 3D[13] ordering, multicomponent diversity,[14] substitutional doping,[15] quasicrystalline order,[16–18] and long-range crystallographic orientation,[19] among others.

One significant limitation of this strategy for the preparation of optoelectronic materials is the insulating nature of the organic surface ligands used to synthetically control the size and shape of the NCs. The organic surface ligands also appear necessary to achieve highly ordered NC assemblies.[20] This requirement is limiting, however, because the ligands present a significant barrier to coupling of electronic states between individual NCs, hampering collective phenomena such as carrier transport, miniband formation, or superradiance. Their insulating nature can be partially mitigated by replacing them with short chain bidentate ligands[21–23] or amorphous inorganic material;[24–26] however, these still prevent the strong coupling necessary for some of the most interesting emergent optoelectronic phenomena.

One way to circumvent the coupling barriers introduced by surface ligands is to eliminate them entirely and chemically fuse the NCs,[27] which if the NCs share the same crystal orientation, can lead to crystallographically coherent NC arrays.[28–30] Fusing the NCs can dramatically increase the conductivity of the arrays indicating strong NC coupling.[30,31] One complication of this strategy is the irreversible nature of the chemical attachment of NCs which can trap structural defects such as dislocations at the interface of imperfectly attached NCs.[32–34] Much like their bulk counterparts, dislocations in imperfectly attached NCs likely introduce undesirable mid-gap trap states.[35,36] Furthermore, disorder in the attached NC superlattice structure, which can prevent carrier delocalization,[37] may also be introduced by dislocations. Thus, the realization of many of the theorized collective properties of attached NC arrays[38,39] will remain elusive until strategies to sufficiently reduce the density of electronically deleterious defects are developed.

Throughout the maturation of the traditional semiconductor industry, deleterious defects have been eliminated to an acceptable level for specific applications.[40,41] Defect elimination was achieved through an unrelenting cycle where “harmful” defects were identified, their formation mechanism understood, and, finally, appropriate changes to the process were developed which lead to their elimination.[42–44] A similar virtuous cycle over the last 25 years has led to the development of semiconductor CdSe/CdS NCs with exceptionally high photoluminescence quantum yields.[45] Without an understanding of the defects present, their electronic and structural consequences, and their formation pathways, it is difficult to devise procedures that prevent defect formation or remove defects from chemically fused NC arrays.

In addition, there are many examples where crystal imperfections have desirable properties and are purposely engineered into materials. One example in semiconductors is the intentional doping of grain boundaries of polycrystalline CdX solar cells or photodetectors with chlorine to engineer p-n junctions at the grain boundaries.[46–50] Another example is the preparation of stacking fault and twin boundary superlattices for quantum well structures.[51–54] Preceding structural defect engineered materials is an understanding of the defect formation mechanisms, their properties and their stability, however in this case the motivation is to identify defects with desirable properties, the process to form them, and the conditions under which they are stable.

To begin to address dislocation formation and stability in imperfect oriented attachment, Ondry et. al. used transmission electron microscopy (TEM) to study the removal pathways of well-defined edge dislocations at the interface of two rock salt PbTe NCs attached on {100} and {110} facets.[55] They found that attachment on {100} facets lead to dislocations with an easy pathway for dislocation removal. On the other hand, attachment on {110} facets resulted in a dislocation that had no easy path to the surface. Two important takeaways, in the context of preparing defect-free materials, from this work are as follows: the primary NCs should be prepared to avoid stepped surfaces as they lead to dislocation formation, and through careful analysis of *in-situ* TEM observing dislocation trajectories, optimal attachment geometries which facilitate dislocation removal can be identified. In a different context, the considerably retarded removal kinetics for imperfect {110} attachment compared to {100} attachment provides an opportunity to engineer stable dislocations in materials which may have desirable properties. While this work provided a framework for how to approach the preparation of dislocation free pairs of NCs, it did not consider the electronic consequences of the attachment or whether and resulting defects will be deleterious to materials performance.

Wurtzite CdSe and CdSe/CdS core/shell NCs are by far the most well-developed semiconductor NC building blocks in terms of material quality,[45] shape control,[56] optical properties,[57] and theoretical understanding.[58] With these considerations in mind, it is desirable to build more complex assemblies out of these prototypical materials. Thus, there is good reason to develop defect resilient oriented attachment strategies for CdX materials. However, the wurtzite lattice is considerably more complex than the rock salt PbX lattice. In terms of dislocations (1D defects), there are 13 distinct perfect dislocations[59] and 18 distinct partial dislocations possible.[60] In addition, there are two distinct classes of stacking faults (2D defects) possible: basal plane stacking faults (which alter the AaBbAaBb stacking sequence)[61] and prismatic stacking faults (PSFs) (which result in a 4/8 member ring structure),[62] both of which can modify electronic structures in these materials.[63,64] Stacking faults present good candidates for preparing metastable defect engineered materials due to their small formation energy, especially for II-VI materials.[65] Further complications arise due to the non-centrosymmetry of the wurtzite lattice which can lead to other planar defects such as inversion domain boundaries.[66] The plethora of possible defects in wurtzite compared to rock salt is a result of the lower symmetry of the lattice and the tetrahedral bonding geometry and thus considerably complicates the considerations for engineering oriented attachment. To begin to consider the attachment of wurtzite NCs, we focus on the nonpolar prismatic facets: the $\{1\bar{1}00\}$ facet and the $\{11\bar{2}0\}$ facet. These arise through cutting the wurtzite lattice with hexagons rotated 30° relative to each other. Synthetically, the $\{1\bar{1}00\}$ facet is typically seen for colloidal CdX NCs,[56,57,67–70] and investigation of the $\{11\bar{2}0\}$ facet and its attachment possibilities has been considerably hampered by the difficulty in preparing $\{11\bar{2}0\}$ facet terminated CdX NCs.

In this paper, we work to develop a detailed understanding of the defects that are formed when colloidal CdSe NCs are chemically attached into crystallographically coherent arrays. Specifically, we characterized the defects that form, their electronic consequences and how easily they can be removed once formed. We successfully prepared well-faceted CdSe NCs terminated with either the $\{1\bar{1}00\}$ or $\{11\bar{2}0\}$ (throughout this work, we use the 4 index Miller-Bravais notation[71] for

hexagonal crystals) prismatic facets, and we demonstrated that a methanolic Na_2Se solution can be used to remove the ligands and chemically fuse the NCs. Using HRTEM, we identified $b = \frac{a}{3}\langle 2\bar{1}\bar{1}0\rangle$ edge dislocations in the case of attachment on $\{1\bar{1}00\}$ facets. In the case of attachment on $\{11\bar{2}0\}$ facets, we observed prismatic stacking faults (PSFs), $b = \frac{a}{2}\langle\bar{1}011\rangle$ partial dislocations bound by a PSF, and $b = \frac{a}{3}\langle 2\bar{1}\bar{1}0\rangle$ edge dislocations at the interface. Next, we evaluated the electronic consequences of the identified defects by performing electronic structure calculations within the semiempirical pseudopotential model. These calculations show the formation of deep hole trap states for $b = \frac{a}{3}\langle 2\bar{1}\bar{1}0\rangle$ edge dislocations and shallow hole trap states in the case of PSFs. Using *in-situ* HRTEM imaging, we identified the pathways these different defects follow as they are annealed out of the NC arrays, and we observed that the dislocations with glide planes leading directly to the surface are much easier to remove. Additionally, we found that interfaces with multiple dislocations are considerably more difficult to remove compared to single dislocations. From this, we propose guidelines for the preparation of attached CdX NCs such as optimal attachment facets, NC assembly tolerances, and superlattice geometry. Altogether, this work constitutes a step towards understanding the defect formation mechanisms, the electronic consequences of defects and the defect healing pathways in attached NCs that is needed to engineer defect resilient materials.

Results

One goal in this work was to determine the ideal facets for attachment of wurtzite CdX (X = S, Se, Te) NCs. In the wurtzite crystal structure, the two most prevalent non-polar low index (energy) prismatic facets which can terminate the crystal are the $\{1\bar{1}00\}$ or the $\{11\bar{2}0\}$ family of facets. To experimentally consider the attachment on these facets, we needed to prepare samples of NCs terminated with the different facets, but still having comparable sizes, crystalline quality, and surface chemistry. Most strategies for preparing wurtzite CdX NCs result in predominately $\{1\bar{1}00\}$ facet termination.[56,57,67–70] To prepare $\{11\bar{2}0\}$ terminated CdSe NCs, we built off the results of Teranishi and co-workers,[72] which showed one of the few examples of $\{11\bar{2}0\}$ terminated colloidal CdX NCs.[73] Using modifications of their chemistry, we were able to synthesize both $\{1\bar{1}00\}$ and $\{11\bar{2}0\}$ terminated CdSe NCs of similar size, crystalline quality, and surface chemistry (see methods section for details). Figure 1A, E show low magnification TEM images of $\{1\bar{1}00\}$ and $\{11\bar{2}0\}$ terminated CdSe NCs, respectively, which show well-defined hexagonal shapes. Both samples had similar size and relatively narrow size distributions, 15.5±2 nm pseudo-diameter for $\{1\bar{1}00\}$ termination and 16±2 nm for the $\{11\bar{2}0\}$ termination, allowing them to readily assemble into hexagonal close packed monolayers with long range orientational order (Figure S4). Figure 1B shows a HRTEM image of a particle viewed down the [0001] zone axis clearly showing the 6 $\{1\bar{1}00\}$ planes terminating the particle – resulting in a well-defined

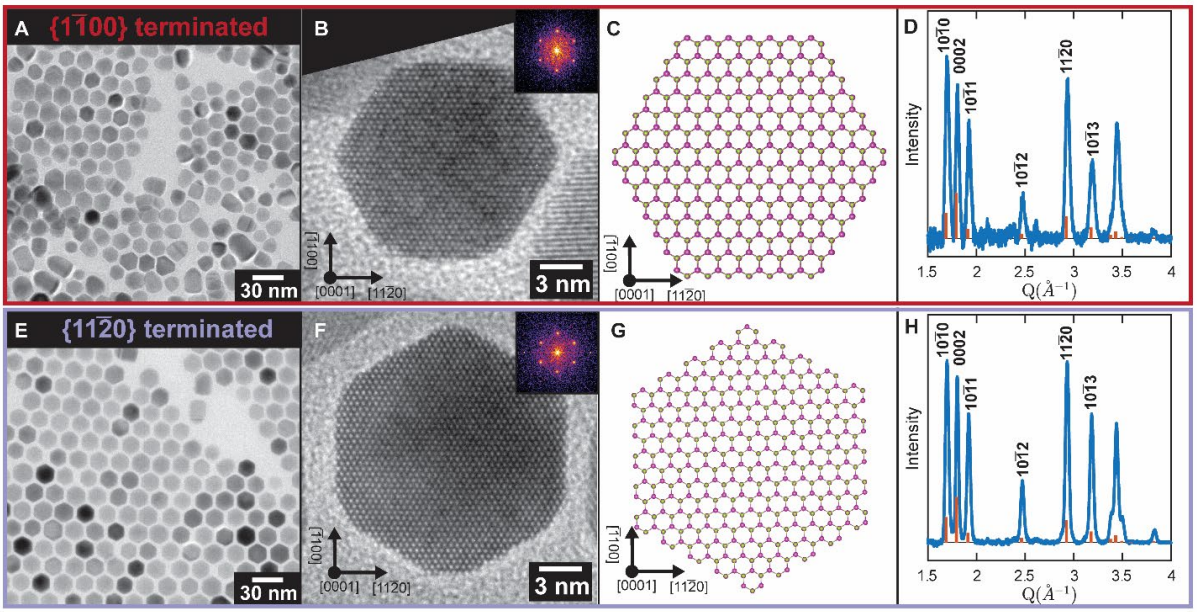

Figure 1. (A)TEM image of {1$\bar{1}$00} terminated CdSe NCs. (B) HRTEM image of a {1$\bar{1}$00} terminated CdSe NC taken down the <0001> zone axis and (C) a model of {1$\bar{1}$00} terminated wz-CdSe shown down the <0001> zone axis. (D) Wide angle XRD from a carefully prepared powder of {1$\bar{1}$00} terminated CdSe NCs with a wurtzite stick pattern (ICSD collection code 415786). (E)TEM image of {11$\bar{2}$0} terminated CdSe NCs. (F) HRTEM image of a {11$\bar{2}$0} terminated CdSe NC taken down the <0001> zone axis and (G) a model of {11$\bar{2}$0} terminated wz-CdSe shown down the <0001> zone axis. (H) Wide angle XRD from a carefully prepared powder of {11$\bar{2}$0} terminated CdSe NCs with a wurtzite stick pattern. HRTEM image (I) and model (J) of 2 wurtzite CdSe particles attached on {1$\bar{1}$00} facets. HRTEM image (K) and model (L) of 2 wurtzite CdSe particles attached on {11$\bar{2}$0} facets.

hexagonal shape. Figure 1C shows a ball and stick model of a wurtzite CdSe NC with {1$\bar{1}$00} termination viewed down the [0001] zone axis. The inset Fourier transform (FT) shows 6 spots corresponding to the {1$\bar{1}$00} planes of the wurtzite lattice. These images were taken under dark-atom contrast conditions, thus the bright dots observed in the HRTEM images correspond to the open channels in the wurtzite lattice. In Figure 1F, we show a HRTEM image of the {11$\bar{2}$0} terminated sample viewed down the [0001] zone axis where the underlying wurtzite crystal has the same orientation relative to Figure 1B. The inset FT of both figures are aligned confirming the same wurtzite lattice orientation for both images. In the {11$\bar{2}$0} case, the sample still adopts a hexagonal shape however it is rotated 30° relative to the hexagonal shape of the {1$\bar{1}$00} terminated sample indicating it is terminated with {11$\bar{2}$0} facets. We note that the {11$\bar{2}$0} terminated samples are truncated by {1$\bar{1}$00} facets to a small extent resulting in a truncated hexagonal shape. Figure 1G shows a ball and stick model of a {11$\bar{2}$0} terminated wurtzite CdSe NC viewed down the [0001] zone axis. Another way to consider the different termination of the two samples is that the {1$\bar{1}$00} facet has a "zig-zag" like termination and the {11$\bar{2}$0} has an "armchair" like termination.

In order to demonstrate the high crystalline quality of the NCs, Figure 1D, H show wide-angle X-ray diffraction patterns for the {1$\bar{1}$00} and {11$\bar{2}$0} terminated samples, respectively, which were carefully prepared as powders to ensure random orientation distribution. Both diffraction patterns contain all the peaks characteristic of wurtzite CdSe (stick pattern) – indicating their similar

crystalline quality. We note that the intensity distributions of the $\{10\bar{1}0\}$, $\{0002\}$, and $\{10\bar{1}1\}$ peaks are different from what is expected for phase pure wurtzite, which can be indicative of stacking disorder, but also from shape effects.[74,75] To confirm the presence of stacking faults, we collected HRTEM images of both the $\{1\bar{1}00\}$ and $\{11\bar{2}0\}$ terminated samples down the $[11\bar{2}0]$ zone axis (Figures S1 A, C). These images confirmed that both samples have basal plane stacking disorder in the form of stacking faults and zinc blende inclusions; however, the samples are still primarily wurtzite with the shape expected for that structure. This is supported by the fact that viewing the samples down the $[11\bar{2}0]$ zone axis reveals that the samples are clearly elongated along the [0001] direction, consistent with the anisotropic reactivity known for wurtzite CdSe.[56,76] Importantly, the samples have similar length distributions, 20±3 nm for the $\{1\bar{1}00\}$ terminated sample and 24±3 nm for the $\{11\bar{2}0\}$ terminated sample. We also collected wide angle powder electron diffraction patterns for samples deposited on carbon TEM grids (Figure S2) to understand the ensemble level crystallographic orientation effects. For the $\{1\bar{1}00\}$ terminated sample, we observed preferential alignment with the [0001] parallel to the substrate, but with a significant portion with the [0001] perpendicular to the substrate. For the $\{11\bar{2}0\}$ terminated sample we see significant alignment with the [0001] perpendicular to the substrate. This alignment is consistent with the orientation preference observed in TEM images of the diffraction area (Figure S3). Based on the detailed structural characterization of these two materials, we have successfully prepared wurtzite CdSe NCs with nearly identical parameters except for the prismatic facets terminating the sample.

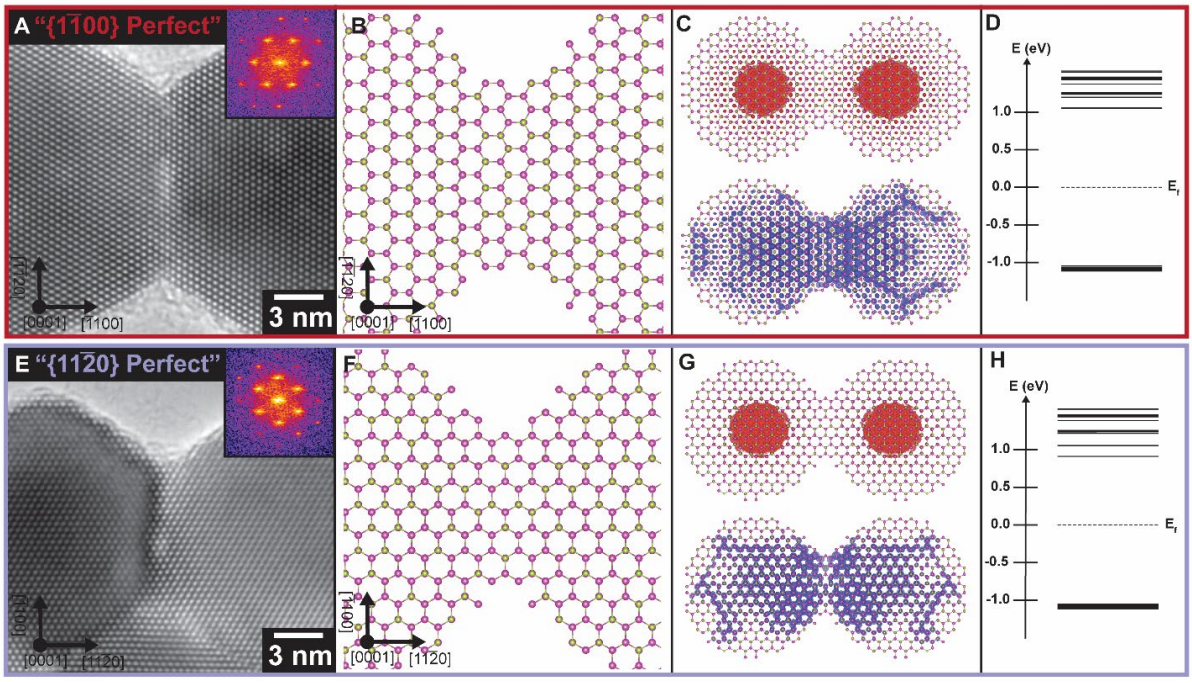

Figure 2. (A, E) HRTEM images and (B, F) models of two wurtzite CdSe NCs attached on $\{1\bar{1}00\}$ and $\{11\bar{2}0\}$ facets, respectively. (C, G) Electron (red) and hole (blue) probability densities including e^- and h^+ interactions for two wurtzite CdSe NCs attached on $\{1\bar{1}00\}$ and $\{11\bar{2}0\}$ facets, respectively. (D, H) Energy level diagrams for the single-particle states attached NCs in C and G, respectively.

Having successfully prepared comparable $\{1\bar{1}00\}$ and $\{11\bar{2}0\}$ terminated CdSe samples, we developed a strategy to induce epitaxial attachment between CdSe NCs. There are many documented approaches for doing this with IV-VI NCs, particularly the PbX (X=S,Se,Te) systems. In these materials, attachment can be induced by heating NC superlattices on a liquid subphase,[34] heating in high vacuum,[77] chemical treatments to remove the organic ligands,[28,29,78] or diluting the particles to desorb surface bound ligands.[55] Ondry et. al. used ligand dilution as an effective means to induce atomically coherent attachment in PbTe NCs for *in-situ* TEM studies.[55] Because the organic ligands are typically more difficult to remove from the surface of CdX and other II-VI materials compared to IV-VI materials,[79] it is harder to induce atomically coherent attachment of CdX NCs. One strategy that has been effective for attaching II-IV materials has been treatment of NC films with dilute methanolic solutions of ammonium sulfide.[80] In this strategy, it is proposed that the S^{2-} ion cleaves the $M(oleate)_2$ bond that tethers the ligands to the surface. This bond cleavage allows the oleate (or other carboxylate ligands) to leave as soluble NH_4-Oleate species. The excess sulfur is incorporated into the inorganic bridge between two adjacent NCs. To circumvent the additional complexity of having multiple chalcogens present, we treated our samples of shape controlled CdSe NCs deposited on carbon or graphene coated gold TEM grids with methanolic solutions of Na_2Se in a glovebox. This treatment successfully led to the atomically coherent attachment of both $\{1\bar{1}00\}$ and $\{11\bar{2}0\}$ terminated CdSe NCs (Figures 2A, E respectively). In both cases, the inset FTs in Figures 2A and 2E show distinct spots indicating atomic coherence across the field of view in the images. Figures 2B and 2F show ball and stick models of the interface that would result between two merged $\{1\bar{1}00\}$ and $\{11\bar{2}0\}$ terminated NCs, respectively. This strategy successfully yielded large arrays of connected NCs with atomic coherence resulting in large (200 x 200 nm) crystals of CdSe (Figure S4).

With a strategy in place to attach wurtzite CdSe on both prismatic facets, we wanted to understand how attachment on the different facets would affect the strength of electronic coupling between quantum confined CdSe NCs. Thus far, the experimental NCs we have shown are too large to exhibit strong quantum confinement effects. Large NCs were used because clear faceting only develops at larger edge lengths, further it facilitates HRTEM investigations and finally, we have been unable thus far to develop a synthetic method to prepare small (<5 nm) $\{11\bar{2}0\}$ terminated CdSe NCs. Nonetheless, it is interesting to consider how the attachment facet may affect the coupling strength between wurtzite CdSe quantum dots. To do this, we performed atomistic electronic structure calculations using the semi-empirical pseudopotential model[81] on two merged NCs attached on either the $\{1\bar{1}00\}$ or $\{11\bar{2}0\}$ facet. Structures were created with a comparable number of planes at their interface and relaxed using molecular dynamics using the Stillinger-Weber interaction potentials for CdSe.[82] We employed the filter-diagonalization technique[83,84] to obtain the noninteracting charge carrier (i.e. electron and hole) eigenstates near the band edge. These noninteracting eigenstates allowed us to compute carrier densities as well as the excitonic (i.e. correlated electron-hole) states by using them as input to the Bethe-Salpeter equation.[85,86] See the Methods section for more details on the molecular dynamics and electronic structure calculations. Figures 2B, F show the interface of the two attached NCs which are attached on the $\{1\bar{1}00\}$ and $\{11\bar{2}0\}$ facets, respectively. Their respective charge carrier probability densities

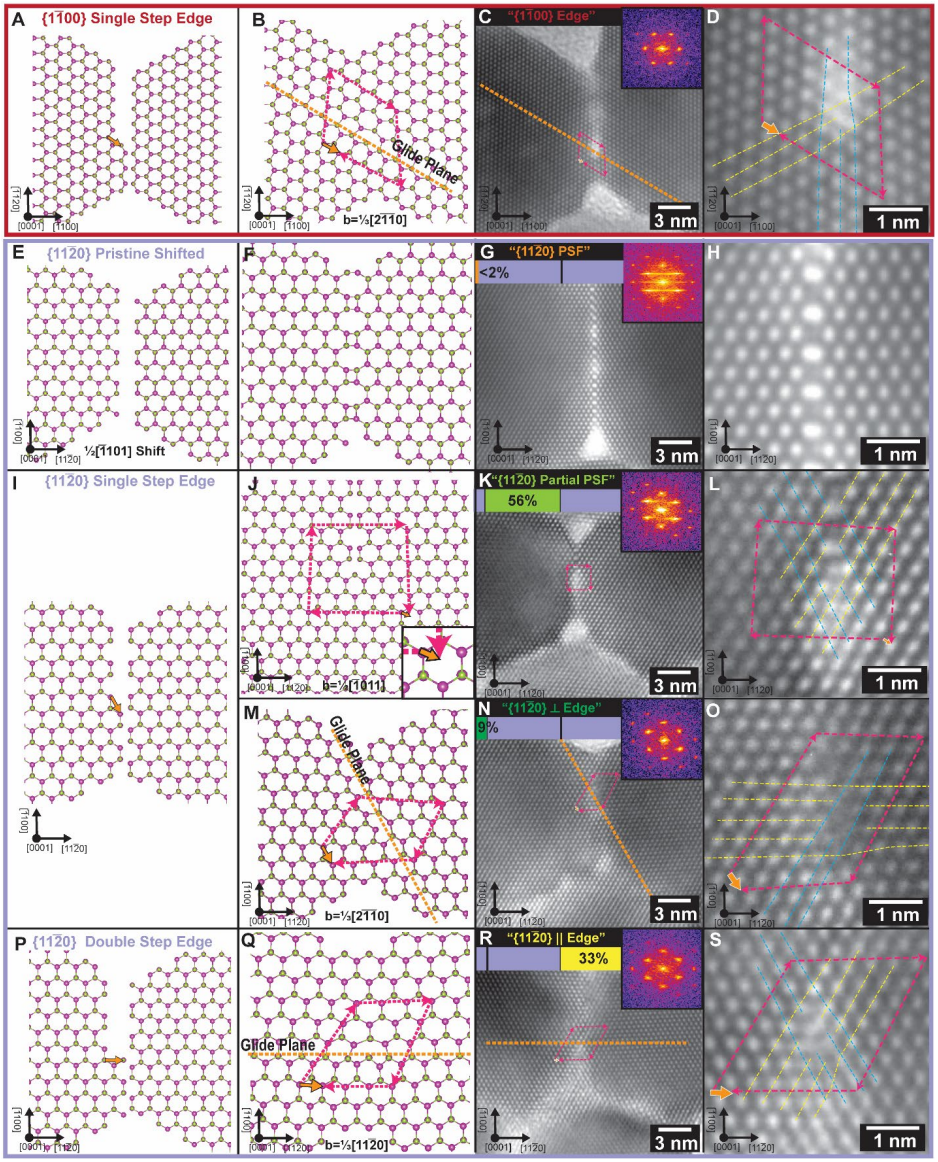

Figure 3. (A) Model of a single step edge on the $(1\bar{1}00)$facet of wz-CdSe and (B) after attaching to a second NC giving rise to a $b = \frac{a}{3}[2\bar{1}\bar{1}0]$ edge dislocation. (C, D) HRTEM image with inset FT of imperfectly attached $\{1\bar{1}00\}$ terminated wz-CdSe particles displaying a $b = \frac{a}{3}[2\bar{1}\bar{1}0]$ edge dislocation. (E) Model of 2 pristine $\{11\bar{2}0\}$ terminated wz-CdSe particles with a $\frac{1}{2}[\bar{1}101]$ shift between the particles and (F) after attaching to create a prismatic stacking fault (PSF) with the $\frac{1}{2}\langle 10\bar{1}1\rangle\{1\bar{2}10\}$ configuration. (G,H) HRTEM with inset FT of imperfectly attached $\{11\bar{2}0\}$ terminated wz-CdSe particles displaying a PSF (I) Model of a single step edge on a $(11\bar{2}0)$facet which after attachment can give rise to either (J) a $b = \frac{a}{2}[\bar{1}011]$ partial dislocation bound by a prismatic stacking fault or (M) a $b = \frac{a}{3}[2\bar{1}\bar{1}0]$ edge dislocation which has a "good" glide plane for removal. (K, L) $b = \frac{a}{2}[\bar{1}011]$ partial dislocation bound by a prismatic stacking fault and (N, O) HRTEM image with inset FT of imperfectly attached $\{11\bar{2}0\}$ terminated wz-CdSe showing a $b = \frac{a}{3}[2\bar{1}\bar{1}0]$ edge dislocation. (P) Model of a double step edge on a $(11\bar{2}0)$facet which after attachment can give rise to (Q) a $b = \frac{a}{3}[11\bar{2}0]$ edge dislocation which has a "bad" glide plane for removal. (R, S) HRTEM image with inset FT of imperfectly attached $\{11\bar{2}0\}$ terminated wz-CdSe showing a $b = \frac{a}{3}[11\bar{2}0]$.

are shown in Figures 2C, G, and their corresponding single-particle energy diagrams are shown in

Figures 2D, H. Both perfectly attached NCs have fundamental gaps of ~2.1 eV, and no mid-gap trapped states are seen in the energy level diagrams. The charge carrier densities, Figures 2C, G, are Boltzmann weighted averages over the lowest energy electron and hole states and show that both carriers are delocalized in both NCs. The electron energy levels and densities can be understood by noting that the two lowest lying electron states exhibit the expected bonding and antibonding level splitting that result from the linear combination of the $1S_e$ electron states of the individual NCs.[87] The hole energy levels and densities are more complicated because of the large hole effective mass in CdSe and large number of hole states that are thermally accessible at room temperature. One consequence of the large hole effective mass relative to the electron mass is that the hole densities (Figures 2C, G) show that the hole has much greater probability of being in the center of the fused NCs compared to the electron. A more detailed analysis of the energy levels and carrier densities will be given later in comparison to the imperfectly attached NCs.

While perfect attachment of NCs is the ideal scenario, it is well known that step edges on the surface of NCs can lead to the formation of dislocations when otherwise perfect NCs undergo oriented attachment.[32,33,88] Recently we showed that the dislocations in imperfectly attached rock salt PbTe NC pairs can be rationally described using dislocation theory.[55] Furthermore, we found that the dislocation dynamics in PbTe NCs were consistent with how dislocations are known to glide in the rock salt lattice. We wanted to test the translatability of dislocation theory to NCs with different lattices. To do this, first we identified the types of dislocations present in the samples of attached wurtzite CdSe NCs. Figure 3A-B shows how a step edge on a $\{1\bar{1}00\}$ facet can give rise to a $b = \frac{a}{3}[2\bar{1}\bar{1}0]$ NCs dislocation. This dislocation has a glide plane that requires the dislocation to glide through the entire NC to be removed from the interface. Figure 3C shows an overview HRTEM image viewed down the [0001] zone axis of an imperfect interface between two $\{1\bar{1}00\}$ terminated CdSe NCs displaying a $b = \frac{a}{3}[2\bar{1}\bar{1}0]$ edge dislocation with an overlaid Burgers circuit and glide plane. A zoomed in HRTEM image of the dislocation core is shown in Figure 3D with an overlaid Burgers circuit. The extra $(1\bar{1}00)$ and $(\bar{1}010)$ planes indicative of a $b = \frac{a}{3}[2\bar{1}\bar{1}0]$ edge dislocation are highlighted in blue and yellow, respectively. In Figure 3B, we show the so-called "full core" structure of the dislocation core which is consistent with what is unambiguously observed in GaN[89] and supported by HRTEM image simulations for CdSe here (Figure S5). For the rest of this paper, we will refer to this dislocation scenario as the "$\{1\bar{1}00\}$ Edge" since the attachment is on the $\{1\bar{1}00\}$ family of facets and it results in an edge dislocation. For $\{1\bar{1}00\}$ terminated CdSe, this was the only type of edge dislocation observed in the case of single dislocations at the interface of the NCs.

In the case of attachment on the $\{11\bar{2}0\}$ facets, four distinct extended defect scenarios were observed. In Figure 3E, we consider the attachment of two pristine $\{11\bar{2}0\}$ terminated NCs, but with a $\frac{1}{2}[\bar{1}101]$ shift between the two particles. This shift gives rise to a prismatic stacking fault (PSF) between the two NCs. PSFs are well-documented in many wurtzite materials[90–93] and have been reported to adopt two configurations, the Amelinkx model with a $\frac{1}{6}\langle 20\bar{2}3\rangle$ displacement[94] and the Drum model with a $\frac{1}{2}\langle\bar{1}101\rangle$ displacement.[90] The latter configuration is more common in

wurtzite semiconductors.[92] Drum model PSFs are characterized by the alternating 8- and 4-member rings in the lattice (Figure 3F) which is qualitatively consistent with the HRTEM images shown in Figures 3G, H. In Figure 3G, we show an overview HRTEM image viewed down the [0001] zone axis showing a PSF that extends across the entire interface between two $\{11\bar{2}0\}$ terminated NCs. The inset FT shows significant streaking of the $(10\bar{1}0)$ and $(01\bar{1}0)$ spots. Streaking in electron diffraction patterns and FT's of HRTEM images are indicative of a stacking error present in a sample.[95] We note that FTs were carefully processed with a Hanning window to avoid streaking artefacts from image edge effects (see methods section). Figure 3H shows a zoomed in HRTEM image of the PSF; the large white dots correspond to the 8-member rings, and the 4-member rings are unresolved in the dark voids. Multislice HRTEM image simulations of the Drum model (Figure S6) compared with the experimental images confirm the Drum structure is observed in our samples. For the remainder of this paper, we will refer to this as the "$\{11\bar{2}0\}$ PSF" extended defect. When considering all the fault errors for $\{11\bar{2}0\}$ attachment, we observe the "$\{11\bar{2}0\}$ PSF" case less than 2% of the time.

Next, we consider structures that can arise from a single step edge on one of the $\{11\bar{2}0\}$ facets (Figure 3I), for which two different extended defect scenarios were observed. First, we discuss the scenario where the stepped surface forms a proper interface, and the recessed surface attaches with a PSF (Figure 3J). This will lead to the formation of a $b = \frac{a}{2}[\bar{1}011]$ partial dislocation which separates the perfect stacking and the PSF. Partial dislocations are characterized by Burgers vectors that do not correspond to a translation vector of the lattice. This can be seen by the [0001] projection of the Burgers circuit where the Burgers vector does not connect two atomic positions (see Figure 3J inset). An example of two joined $\{11\bar{2}0\}$ terminated particles with a PSF across part of the interface is shown in Figure 3K. The streaking of the $(10\bar{1}0)$ and $(01\bar{1}0)$ spots in the FT is also observed indicating the presence of a PSF in the image. Figure 3L shows a zoomed in HRTEM image of the dislocation core showing how the $(01\bar{1}0)$ and $(10\bar{1}0)$ planes (blue and yellow, respectively) merge perfectly at the bottom of the image and have a stacking error at the top of the image. In Figure 3J, we show the "full core" structure of the partial dislocation, however an open core structure is also possible (Figure S7). We attempted to identify the structure by comparing with multislice HRTEM image simulations (Figure S7) and the full core structure seems more plausible; however, we were unable to unambiguously determine the structure due to the limited resolution of our TEM. Unfortunately, we could not find literature reports of the core structure of this partial dislocation determined by more reliable techniques such as aberration corrected HAADF-STEM imaging. Despite this, our results clearly indicate that $b = \frac{a}{2}[\bar{1}011]$ partial dislocations can exist at the interface between CdSe NCs attached on the $\{11\bar{2}0\}$ facet. Furthermore, we observe this dislocation scenario, which we will call the "$\{11\bar{2}0\}$ Partial PSF", in 56% of the defective interfaces for attachment on the $\{11\bar{2}0\}$ facet.

In the second case of $\{11\bar{2}0\}$ attachment with a single step edge, a full edge dislocation is formed at the interface again with a $b = \frac{a}{3}[2\bar{1}\bar{1}0]$ Burgers vector. This is shown in Figure 3M with overlaid Burgers circuit and glide plane. Figure 3N shows an overview HRTEM image of two joined $\{11\bar{2}0\}$ terminated CdSe particles with a $b = \frac{a}{3}[2\bar{1}\bar{1}0]$ edge dislocation at the interface.

This dislocation has the same Burgers vector and dislocation structure as described previously for the "$\{1\bar{1}00\}$ Edge" scenario, however its relationship relative to the attachment direction is rotated by 30°. In this case, the glide plane of the dislocation quickly intersects the surface which should allow for easier dislocation removal. In Figure 3O we show a zoomed in image of the dislocation core and highlight the extra $(\bar{1}010)$ and $(1\bar{1}00)$ planes in blue and yellow, respectively. We will refer to this dislocation, which we observe 9% of the time, as the "$\{11\bar{2}0\} \perp$ Edge" because it results from attachment on $\{11\bar{2}0\}$ facets and has a glide plane nearly perpendicular to the attachment direction.

Finally, we consider the case of a double step edge on the $\{11\bar{2}0\}$ facet shown in Figure 3P. This case also leads to a $b = \frac{a}{3}\langle 2\bar{1}\bar{1}0\rangle$ type edge dislocation that is related by symmetry to the other edge dislocations. Specifically, in this case, using the same indexing conventions as the other dislocation cases, it has a $b = \frac{a}{3}[11\bar{2}0]$ Burgers vector (Figure 3Q) and associated glide plane which is co-linear with the attachment direction. Figure 3R shows an overview HRTEM image of an interface between two particles attached on the $\{11\bar{2}0\}$ facet displaying a $b = \frac{a}{3}[11\bar{2}0]$ edge dislocation with overlaid Burgers circuit and glide plane. Figure 3S shows a zoomed in HRTEM image of the dislocation core with the overlaid extra $(01\bar{1}0)$ and $(10\bar{1}0)$ planes (blue and yellow, respectively) planes characteristic of the edge dislocation. This dislocation scenario, which we will call the "$\{11\bar{2}0\} \parallel$ Edge" since the glide plane is co-linear with the attachment direction, was observed 33% of the time for imperfect attachment events on the $\{11\bar{2}0\}$ facet. One interesting observation is how the step vector describing the surface step that would lead to each of the different edge dislocation scenarios (orange arrow in Figures 3A, I, and P) corresponds exactly with the Burgers vector of the various dislocations observed. The five extended defect cases for the two attachment facets presented here represent all those that we observed; however, it is important to remember that in this orientation, screw dislocations are not easily observed by HRTEM and may be present in our samples.

Having identified the dislocation structures present after oriented attachment, we wanted to elucidate which dislocations would have deleterious electronic consequences. To this end, we performed electronic structure calculations using the semi-empirical pseudopotential method as described above (and in detail in the Methods section) on the imperfectly attached NCs (i.e. fused NCs with the observed dislocations at the interface of the two NCs). The calculation results for the "$\{11\bar{2}0\}$ PSF" and the "$\{11\bar{2}0\} \parallel$ Edge" are shown in Figure 4. Localized mid-gap trap states were identified for both defective structures, with the energy level diagrams of the single-particle states shown in Figures 4B, F. We assign a deep or shallow label to such trap states (red and orange respectively), with the former only present in the $\{11\bar{2}0\} \parallel$ Edge scenario. The Fermi level (E_f) for Figures 4B, F were taken from the perfect attachment calculation shown in Figure 2D, which is the calculated midpoint of the band gap (E_g) for two NCs that had undergone perfect oriented attachment at the $\{11\bar{2}0\}$ facet.

For both the "$\{11\bar{2}0\}$ PSF" (Figures 4C, D) and "$\{11\bar{2}0\} \parallel$ Edge" (Figures 4G, H), a Boltzmann weighted average of the charge densities of the lowest energy states show localization of the hole at the crystalline interface. This is independent of whether the hole is the only charge carrier in the

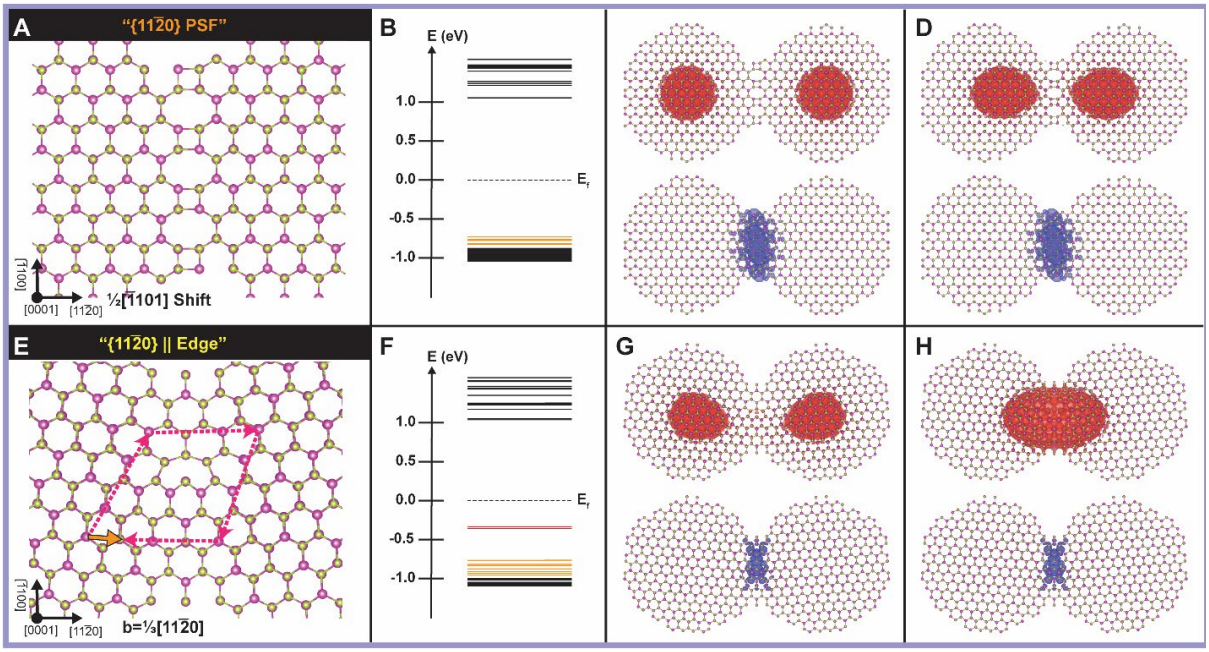

Figure 4. Electronic structure calculations of attached quantum dots with a (A-D) $\{11\bar{2}0\}$ PSF interfacial defect and (E-H) "$\{11\bar{2}0\}$ ∥ Edge" interfacial defect. (A, E) Interface of the attached particles used in electronic structure calculations, with a Burgers circuit included in (E). (B, F) Energy level diagrams (in eV) for the single-particle states. Defect related shallow and deep hole trap states are shown in orange and red, respectively. The Fermi energy, E_f, was chosen to be the midpoint of the calculated fundamental gap, E_g, for the attached quantum dots that underwent perfect oriented attachment on the $\{11\bar{2}0\}$ facet. (C, D, G, H) Electron (red) and hole (blue) probability densities for (C, G) the single-particle (i.e. noninteracting electron and hole) states and (D, H) the excitonic (i.e. correlated electron-hole) states. All probability densities are shown at the same isosurface value and are Boltzmann weighted averages over the low energy (C, G) single-particle and (D, H) excitonic states.

fused NC or if the hole is interacting with an electron, as would be the case if the hole was generated *via* photon absorption. For the PSF, localization occurs at the 4- and 8- membered ring motif at the interface and, for the "$\{11\bar{2}0\}$ ∥ Edge", the deep hole trap states are restricted to the dislocation core of the "$\{11\bar{2}0\}$ ∥ Edge". Interestingly, the charge probability densities for the electron states display clear differences between the charge excitation (noninteracting) picture (Figures 4C, G) and neutral excitation (interacting) picture (Figures 4D, H) charge densities. In the charged excitations, the electron probability densities are segregated: an interfacial node separates the electron density of each particle (Figures 4C, G). When allowed to interact with hole states in the neutral excitation case, the electron densities for both structures are brought closer to the hole (Figures D, H). However, Figure 4D shows that for the "$\{11\bar{2}0\}$ PSF", the electron density still avoids the interface. This is contrasted by the "$\{11\bar{2}0\}$ ∥ Edge" in Figure 4H, where the electron and hole probability densities of the lowest energy excitonic states are localized at the dislocation core. Similar hole localization and subsequent electron localization in the interacting case were observed for the "$\{1\bar{1}00\}$ Edge" and "$\{11\bar{2}0\}$ ⊥ Edge" cases (Figure S8). Compared to perfect attachment in Figure 2, structural defects at the interface lead to mid-gap trap states which could negatively impact the performance of devices based on chemically fused NCs.

In the context of realizing delocalized electronic states, the extended defects have many negative consequences, and thus we consider the prospects for removal of these defects. In rock

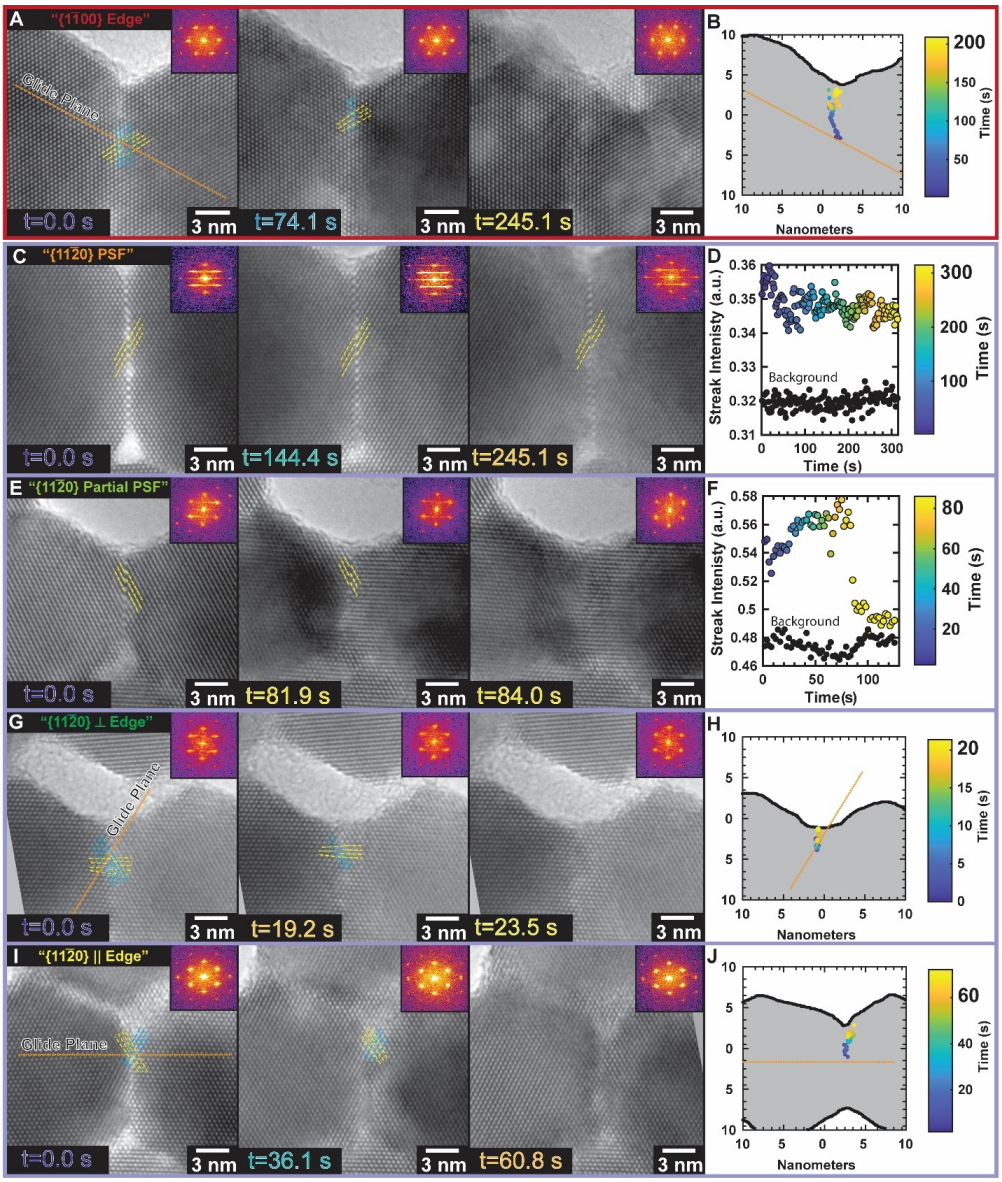

Figure 5. (A) Timeseries of images as a $b = \frac{a}{3}[2\bar{1}\bar{1}0]$ edge dislocation anneals out of the interface between two $\{1\bar{1}00\}$ terminated particles. (B) Position of the dislocation in each frame determined by the discontinuity in the strain field measured by geometric phase analysis. (C) Timeseries of images with inset FTs as a perfect PSF between two $\{11\bar{2}0\}$ terminated particles is electron beam annealed with a dose rate of ~5000e$^-$/Å^{2}s. (D) Plot of the streak intensity in the FT of each frame, which is a characteristic of stacking errors, as a function of time while the PSF is electron beam annealed. The background intensity (black) is from a nearby part of the image without a PSF present. (E) Timeseries of images as a $b = \frac{a}{2}[\bar{1}011]$ dislocation bound by a prismatic stacking fault anneals out of the interface between two $\{11\bar{2}0\}$ terminated particles. (F) The intensity of the streak in the FT which signifies the presence of a PSF as a function of time. (G) Timeseries of images as a $b = \frac{a}{3}[2\bar{1}\bar{1}0]$ edge dislocation anneals out of the interface between two $\{11\bar{2}0\}$ terminated particles with the position of dislocation in each frame shown in (H). (I) Timeseries of images as a $b = \frac{a}{3}[11\bar{2}0]$ edge dislocation anneals out of the interface between two $\{11\bar{2}0\}$ terminated particles with the position of dislocation in each frame shown in (J). For all plots, the time is shown by the colorbar, but each trajectory has a different timescale. Gray shading in the plots indicates the NC outline.

salt PbTe, we previously observed that a dislocation with a glide plane which quickly intersected

the surface is much easier to remove compared to ones that do not.[55] In this work, we again performed electron dose rate controlled *in-situ* TEM experiments,[96] which can qualitatively simulate thermal annealing,[97,98] to observe the dislocation dynamics in imperfectly attached NCs. Figure 5 overviews the dislocation removal pathways for the five dislocation scenarios observed. Figure 5A shows snapshots from a timeseries of HRTEM images (Video S1) showing the pathway a "$\{1\bar{1}00\}$ Edge" dislocation follows as it is expelled from the interface at the surface. Figure 5B shows the position of the dislocation, determined by image analysis techniques (see methods), in each frame as a function of time. The dislocation moves out of its glide plane generally in the $[11\bar{2}0]$ direction which has both glide (movement ∥ to glide plane) and climb (movement ⊥ to glide plane) character. The dislocation takes nearly 200 seconds to reach the surface, and the relatively slow kinetics is consistent with a process needing dislocation climb, which requires vacancies to coalescence with the dislocation for it to move out to its glide plane.

Next, we consider the "$\{11\bar{2}0\}$ PSF" scenario. Snapshots from a timeseries of TEM images are shown in Figure 5C and the full movie is shown in Video S2. In this case, even after over 245 seconds of electron beam stimulation, signatures of the PSF are still present both in the image and manifested as streaks in the FTs for each frame. Analysis of the streak intensity (see methods section for details) in the FT for each fame (Figure 5D), which indicates the presence of a PSF shows that the defect is not removed during the observation period. Thus, it seems that the PSF interface is very stable and difficult to remove. On the other hand, when the PSF is terminated with a partial dislocation, the "$\{11\bar{2}0\}$ Partial PSF" case (Figure 5E and Video S3), we observe that the PSF spontaneously and quickly heals compared to the "$\{11\bar{2}0\}$ PSF" scenario. This can be further illuminated by plotting the FT streak intensity of each frame as a function of time (Figure X2) which shows higher intensity than the background initially, then abruptly (<2 s) returns to the background levels when the defect is removed. These observations suggest that the presence of a partial dislocation facilitates the removal of PSFs from the interfaces between $\{11\bar{2}0\}$ terminated nanoparticles.

Finally, we consider the two distinct edge dislocations that form during the attachment of $\{11\bar{2}0\}$ terminated nanoparticles. In the case of the "$\{11\bar{2}0\}$ ⊥ Edge", we observe that the dislocation is removed from the material faster than all the other defects (Figure 5G and Video S4). Tracking the dislocation position in each frame (Figure 5H) shows that, as expected, the dislocation follows its glide plane to the surface where it is annihilated. In the "$\{11\bar{2}0\}$ ∥ Edge" scenario (Figure 5I and Video S5), the dislocation does not have a glide plane that leads directly to the surface or, in this specific case, the void that exists in at the node of 3 nanoparticles. Figure 5J shows that the dislocation undergoes climb to move out of its glide plane and, importantly, takes approximately 3 times longer to travel an almost identical distance as the "$\{11\bar{2}0\}$ ⊥ Edge" case. These findings clearly highlight the importance of the orientation of the glide plane relative to the surface for edge dislocation removal and are consistent with our previous observations in PbTe.[55]

We also observed situations where multiple dislocations formed at the interface of $\{1\bar{1}00\}$ and $\{11\bar{2}0\}$ terminated particles shown in Figures 6A, B and C, D, respectively. In one observed case of multiple edge dislocations resulting from $\{1\bar{1}00\}$ attachment, we see two edge dislocations with $b = [2\bar{1}\bar{1}0]$ (top) and $b = [\bar{1}2\bar{1}0]$ (bottom) Burgers vectors and associated glide planes (Figure

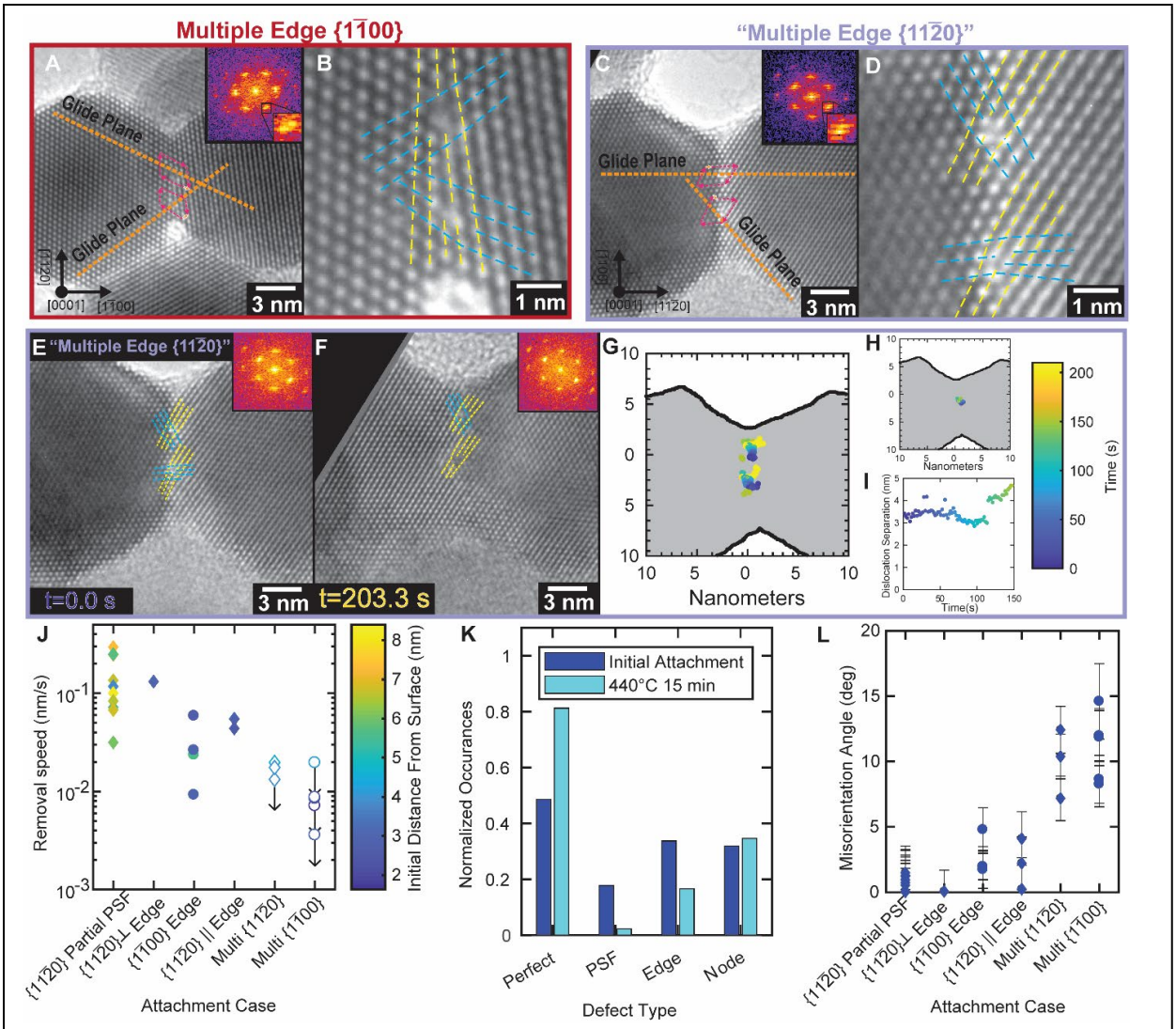

Figure 6. (A) Overview HRTEM image of the imperfect interface between two {1$\bar{1}$00} terminated CdSe particles which has two dislocations overlaid with the Burgers circuits and glide planes. (B) Zoomed in view of the dislocation cores with the 2 extra (10$\bar{1}$0) planes in yellow and extra (1$\bar{1}$00) and (01$\bar{1}$0) planes highlighted in blue. (C) Overview HRTEM image of the imperfect interface between two {11$\bar{2}$0} terminated CdSe particles which has two dislocations overlaid with the Burgers circuits and glide planes. (D) Zoomed in view of the dislocation cores with the 2 extra (10$\bar{1}$0) planes in yellow and extra (1$\bar{1}$00) and (01$\bar{1}$0) planes shown in blue (E) initial structure of {11$\bar{2}$0} attachment with 2 edge dislocations and the same NCs (F) after considerable electron beam annealing. (G) The position of the two dislocations with time, (H) the center of mass of the two dislocations and (I) the separation between the two dislocations as a function of time. (J) Average removal speeds for the different dislocation classes of attachment. The color of each dot represents how far the dislocation was from the surface initially. Filled dots represent dislocations which annealed out in the observation time, and open circles did not, thus the removal speed is only an upper bound. (K) Number of interface types observed in a sample of {11$\bar{2}$0} attached CdSe before and after annealing the sample at 440°C in vacuum for 15 min. the plot was normalized to the sum of perfect, PSF, and edge interfaces. Node refers to a defect at the node where 3 particles touch. (L) Misorientation angle between the two NCs for each attachment case in the different dislocation classes

6A) which show a complicated geometry. Figure 6B shows the detailed structure near the dislocation cores. The dislocation cores are separated by ~2.5 nm. In the case of multiple dislocations at interfaces, the exact geometries of the Burgers vectors and the glide planes were

unique in each case, even for the same attachment facet. The presence of multiple dislocations resulted in larger mistilt between the two attaching quantum dots; the evidence of the mistilts is the two distinct $\{1\bar{1}00\}$ peaks in the FT which are further highlighted by the FT inset.

The case of multiple dislocations at the attachment interface of two $\{11\bar{2}0\}$ terminated particles is shown in Figure 6C. In this specific case, we observe edge dislocations with $b = \frac{a}{3}[11\bar{2}0]$ (top) and $b = \frac{a}{3}[2\bar{1}\bar{1}0]$ (bottom) Burgers vectors with their associated glide planes overlaid on Figure 6C. Figure 6C shows the detailed structure at the dislocation cores which are separated by ~3 nm in this $\{11\bar{2}0\}$ case. We also observed a variety of specific geometries for multiple dislocations at $\{11\bar{2}0\}$ interfaces.

To understand the effects on removal kinetics that multiple dislocations have, we observed the dislocation trajectories of the "Multiple Edge $\{11\bar{2}0\}$" scenario during electron beam annealing and found that even after 250 s of annealing time, the defects made little progress to the surface (Figure 6E-F and Video S6). The position of the two dislocations was determined for each frame and their positions are plotted in Figure 6G with color corresponding to the time. We observe the dislocations make little progress to the surface. The center of mass of the two dislocations (Figure 6H) also shows little movement to the surface. Furthermore, the distance between the two dislocations remains relatively constant over the first 120 seconds of the trajectory until it abruptly increases. This change happens concurrently with an abrupt decrease in the image quality; thus, it is difficult to discern if the abrupt change is real. We also saw significantly slower defect removal in the case of multiple dislocations at the interface of $\{1\bar{1}00\}$ terminated particles (Video S7). Based on these trajectories, it is clear that the addition of a second dislocation at an interface greatly hampers the system's ability to heal those dislocations.

While the individual trajectories are illuminating about the mechanisms of dislocation removal, it is important to verify that the trends observed hold across multiple attachment events. In Figure 6J, the dislocation removal speed, which we defined as the distance the dislocation had to move to be removed divided by the time it takes for removal, is shown for many different trajectories in each defect category. Because dislocation surface attractive forces can have an effect on the kinetics,[55] we differentiate the initial distance the dislocation was from the surface by the color of the point on the graph. In this plot, the full circles indicate that the dislocations were removed during the observation time and the open circles indicate that the dislocations were not successfully removed from the interface, thus, giving an upper bound for the dislocation removal speed. It is important to note that all the data was collected at the same dose rate which was carefully calibrated in a self-consistent manner for each experiment (see methods). In Figure 6J, we arrange the dislocation categories by increasing removal difficulty (slower removal speed) from left to right. Based on removal speed, the "$\{11\bar{2}0\}$ Partial PSF" and "$\{11\bar{2}0\}$ $\perp$ Edge" provide the best prospects of removal. The "$\{11\bar{2}0\}$ $\parallel$ Edge" and "$\{1\bar{1}00\}$ Edge" provide similar prospects for dislocation removal, especially when considering that the specific dislocation trajectories were a bit larger in the "$\{1\bar{1}00\}$ Edge" case than in the "$\{11\bar{2}0\}$ $\parallel$ Edge" case. Finally, we observe that in either attachment facet, when more than one dislocation is at the interface, the dislocation removal was significantly slowed. In seven cases with two or more defects at the interface, all of

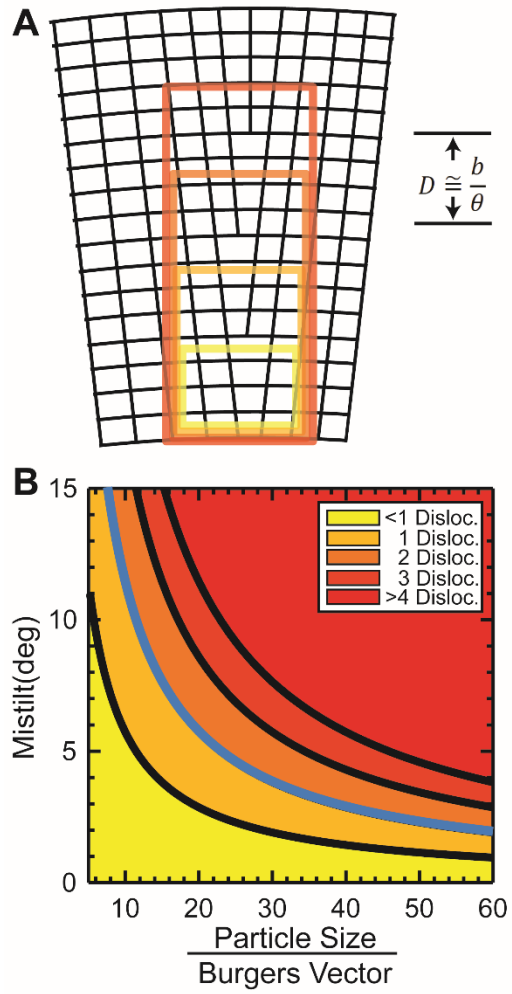

Figure 7. (A) A low angle tilt boundary between two crystals where for low tilt angles, the dislocation is given by the equation. The colored boxes represent different sized NCs attaching with a given mistilt, which can be thought of different sized snapshots of the low angle tilt boundary. (B) Plot showing the number of dislocations expected at a NC interface as a function of mistilt angle and particle size normalized by the Burgers vector of dislocations at that interface. Different colors represent how many edge dislocations would be expected for a given particle size and mistilt.

them were stable during the observation time (>200 s), which was as long, if not longer than all the cases where successful removal was observed.

Thus far in this work, the dislocation dynamics were stimulated with the electron beam, yet thermal annealing would likely be used to drive dislocations out of these materials in a synthetic procedure. To determine if dislocation removal kinetics for thermal annealing are qualitatively consistent with our observations, we compared the interface dislocation densities before and after annealing a sample of NCs attached on $\{11\bar{2}0\}$ facets at 440° C for 15 min in a TEM column vacuum using a heating holder. We simplified our comparative analysis to include perfect interfaces, defects with edge character, and defects with PSF character (either partial or full). Figure 6K shows the prevalence of perfect, edge, and PSF dislocations before (dark blue) and after (light blue) annealing the sample. Initially, ~50% of the interfaces are perfect with the rest having either a PSF (20%) or an edge dislocation (30%). After annealing, over 80% of the interfaces are perfect with ~18% containing an edge dislocation, and ~2% of the interfaces have a PSF defect. These results are qualitatively consistent with the observations in Figure 6J that the partial PSF are the easiest to remove, and all the different cases of edge dislocations are more difficult to remove. Furthermore, the only remaining PSFs after the annealing were the case of the PSF across the entire interface (Figure S9), consistent with our observation that full PSF are stable. Finally, we observed defects that at the confluence of three particles (labeled "Node" in Figure 6K). There were a significant number of defects at the 3-particle intersection, but their concentration did not significantly change after annealing. Altogether, the dislocation and stacking fault concentration changes upon thermal annealing are consistent with our single particle kinetic observations.

A simple metric for quantifying the degree of error in the attachment process is the misorientation angle between the two crystallites. We plot the misorientation angle for all the dislocation classes considered in the previous panel in Figure 6H. Unsurprisingly, the multiple dislocation cases have the largest average misorientation angle of ~11°. The single edge

dislocation cases have on average a ~3° misorientation angle and the "{11$\bar{2}$0} Partial PSF" had a ~1° misorientation angle. The defective boundary between two NCs can be thought of as a small snapshot of a low angle tilt boundary. In this context, the number of dislocations per unit length is directly related to the mistilt angle.[99] Figure 7A shows a low angle tilt boundary for an idealized cubic lattice where the dislocation spacing, D, depends on the Burgers vector, b, and mistilt, θ, according to equation 1.

$$D \cong \frac{b}{\theta} \quad eq.1$$

The different shades of orange outline what can be thought of as NCs of different sizes having imperfect interfaces for a fixed mistilt angle. In the case of the smallest interface, zero dislocations at the interface are expected. As the size of the NC increases, an increasing number of dislocations are expected along the interface. We make this more quantitative by calculating the number of dislocations at an interface for a given NC size normalized by the Burgers vector magnitude and mistilt angle. Figure 7B shows the results of this analysis; we immediately see that smaller NCs can tolerate larger mistilts before increasing the number of dislocations. We emphasize the cutoff between one and two dislocations at the interface with a blue line, because staying to the left of this line will avoid the formation of multiple dislocations which we observed to greatly hamper dislocation removal (Figure 6J). This simple analytic model provides general guidelines for the angular alignment required to achieve attached NCs for which the defects can be more easily removed.

Discussion

We consider the implications of this work for those interested in attached assemblies of nanocrystals and their electronic properties. In the first section, we discuss the removal dynamics of the dislocations themselves in CdSe. In the second section, we consider the electronic consequences of dislocations in CdSe and discuss ways to mitigate them. Next, we compare the relative merits of attaching wurtzite CdSe on the {1$\bar{1}$00} and {11$\bar{2}$0} facets by considering the synthesis of starting materials, dislocation formation, electronic consequences, and dislocation removal. Then, using the insights gleaned from individual NC attachment, we suggest ideal attachment geometries and assembly tolerances necessary to achieve high quality arrays of attached NCs. Finally, we generalize our results to NC attachment of arbitrary materials and connect them to other material growth mechanisms.

Understanding dislocation removal mechanisms in imperfectly attached CdSe.

An improved understanding of the removal mechanisms of edge dislocations and prismatic stacking faults is important for this area to advance from strictly empirical to a more predictive approach. The mechanisms themselves vary considerably, depending on the precise local structure of any defects, the orientation of the glide lane relative to the surface, the number of dislocations at the interface, and the possible presence of chemical species at the surface that may be incorporated into the interface upon attachment. In what follows, we discuss the various cases that arise starting first with single edge dislocations, then multiple edge dislocations, followed by PSFs and finally the presence of impurities.

Starting with the simplest case of the perfect edge dislocation scenarios, even here we see that there are various outcomes, depending on the orientation of the glide plane with respect to the surface where the defect can be removed. This changes the relative amounts of climb and glide character needed to remove the dislocations. The "$\{11\bar{2}0\} \perp$ Edge" dislocation has a removal path with pure glide character while such a pathway does not exist for the "$\{11\bar{2}0\} \parallel$ Edge" dislocation. The "$\{1\bar{1}00\}$ Edge" dislocation is in the intermediate regime with both climb and glide character. Based on our kinetic observations, dislocations that require climb for removal are slower and, thus, should be avoided if the goal is to prepare defect free materials. This observation in wurtzite CdSe supports the generality of our previous observations in PbTe.[55] Later we will discuss the feasibility of avoiding dislocations which need climb for removal in the specific case of wurtzite CdSe.

One interesting observation is that the presence of two or more dislocations at the interface greatly hinders dislocation removal. We now consider why it might be that two nearby dislocations can be expected in principle to be much more difficult to remove than a single isolated one. The approach of a single dislocation to the surface can be described as arising by a force between the dislocation and an opposite sense image dislocation present in the vacuum.[99] Because of the highly non-linear nature of the surface image force on a single dislocation at an interface, the forces only cancel out if the dislocation is in the exact center, which is mechanically unstable.[100] In the case of two real dislocations at the interface, there are now elastic interactions between both the real and image dislocations. Depending on the exact geometry of the real dislocations, they can be attracted to each other, repelled, or held at an equilibrium distance from each other.[99] These interaction forces can cancel out the image forces which attract the dislocation to the surface leading to hindered removal. A detailed examination of the elastic interactions and the precise dislocation geometries that can retard removal is beyond the scope of this work (and would likely require detailed finite element modeling). Nonetheless, the basic idea that the strain fields of multiple dislocations at an interface interact and can suppress removal provides a qualitative understanding for the considerably slowed defect removal of multiple interfacial dislocations.

The simple glide versus climb picture does not apply for prismatic stacking faults. We observed that when a PSF is terminated by a $b = \frac{a}{2}[\bar{1}011]$ partial dislocation ("$\{11\bar{2}0\}$ Partial PSF"), the PSF and corresponding partial dislocation are easily removed, whereas a "$\{11\bar{2}0\}$ PSF" is remarkably stable. At first glance, this is consistent with the role partial dislocations play in facilitating basal plane stacking sequence changes during wurtzite/ zinc blende phase transitions where nucleated partial dislocations easily move across the basal planes while changing the stacking sequence.[101] If this mechanism were in play here, we would expect to see the partial dislocation move towards the surface and the length of the PSF would become gradually shorter. However, we observe a nearly constant length of the PSF (Figure S10) throughout the annealing and, thus, no movement of the partial dislocation up until removal. Furthermore, we observe a constant streak intensity until the streak returns to the background level within a single frame (Figure 5F), indicating an unusually rapid (sub 2 s) defect removal. Therefore, simple partial dislocation migration to the surface is inconsistent with our observations, and we suspect the mechanism of $b = \frac{a}{2}[\bar{1}011]$ partial dislocation/ PSF removal is more complicated. One possibility is that the PSF first folds over to become a basal plane stacking fault separated by a $b = \frac{a}{6}[10\bar{1}0]$ stair-rod dislocation. The movement of this stair rod dislocation along the [0001] direction could

lead to rapid removal of the PSF as it exits the top or bottom surface of the NC film, consistent with the sudden removal of the "$\{11\bar{2}0\}$ Partial PSF" we observed. Unfortunately, direct observation of this would be difficult since it requires viewing down the $[11\bar{2}0]$ zone axis, which requires a 90° rotation of our sample in its current geometry, something infeasible at present in a TEM. Nonetheless, we speculate the presence of a $b = \frac{a}{2}[\bar{1}011]$ partial dislocation may facilitate the movement of the stair-rod dislocation which allows the removal of "$\{11\bar{2}0\}$ Partial PSF" dislocations and not "$\{11\bar{2}0\}$ PSF" dislocations.

Finally, it is interesting to consider the role that surface impurities may have on dislocation motion in CdSe. It has been well established that chlorine, either from Cl terminated NCs or $CdCl_2$ treatments of films, is a grain growth and wurtzite/zinc blende phase transition promoter in CdX thin film processing.[46–49,102] This indicates that Cl facilitates atom rearrangement in CdX materials, and we suspect that Cl may also influence dislocation removal kinetics. In particular, Cl may facilitate dislocation motion since the wurtzite/zinc blende phase transition proceeds *via* partial dislocation motion to alter the stacking sequence.[101] In our work, the NCs likely have some amount of Cl on the surface from the Cetyltrimethylammonium chloride (CTAC) used to prepare the $\{11\bar{2}0\}$ terminated samples. We were careful to ensure that NCs with both $\{1\bar{1}00\}$ and $\{11\bar{2}0\}$ facets were prepared using similar chemistry, particularly the presence of CTAC, to ensure impurities had similar effects on the dislocation dynamics for the different facets. It would be interesting to understand the role of impurities on extended defect removal in Cl terminated CdSe and non-Cl terminated CdSe. Considering the vast chemistry available for surface modification in colloidal NCs, surface impurity introduction may be an additional tool to facilitate defect removal after imperfect oriented attachment. The understanding of dislocation motion in CdSe determined by *in-situ* TEM will be used in the subsequent sections to identify ideal attachment facets for wurtzite NCs.

Understanding and mitigating electronic consequences of dislocations and PSF's in CdSe.

Given the small size and large surface to volume ratio of nanocrystals, materials produced through attachment processes are likely to produce a very high density of electronic defects, at least initially. Thus, the question of identification and if possible mitigation of attachment induced electronic defects is central to the viability of these materials for optoelectronics uses. In many crystalline inorganic semiconductors, some dislocations have negative consequences while others are electronically inactive or can be rendered inactive through appropriate doping. In the case of perfect edge dislocations (Figure 4 and Figure S8), we observe the formation of deep hole trap states. The observation of deep trap states for $b = \frac{a}{3}\langle 2\bar{1}\bar{1}0\rangle$ edge dislocations is qualitatively consistent with what has been calculated for GaN,[103] and the observation of shallow hole traps for PSFs is also consistent with GaN.[63] Phenomenologically this is consistent with the ease of hole trapping in CdSe on un-passivated chalcogen atoms.[104] While not explicitly considered here, the stoichiometry of the dislocation core (determined by the chemical potential of the components during growth) can have a considerable impact on the electronic properties and may represent a pathway to render dislocations electronically harmless.[103] Further small impurities such as hydrogen have been speculated to passivate dislocations cores in GaN. Finally, modulation of the Fermi level through impurity doping can fill dislocation states rendering them inactive. All these

factors could be optimized in the future to render harmful defects inactive or at least minimize their influence in attached NC-based materials.

One interesting observation in the case of the "$\{11\bar{2}0\}$ PSF" is that the electron states avoid the 4- and 8- member ring motif of the PSF in both the noninteracting case, and the interacting case, even though the localized holes at the interface provide a strong Coulomb driving force for electron localization (see for example the edge cases Figure 4D). To understand the reason for this, we recall that the electron wavefunction of a state in an individual NC can be modeled as the product of the S-like envelope function and the Bloch wavefunction at the bulk semiconductor band edge.[105] For a carrier to delocalize across an interface, the phase relationship between the Bloch functions of the two NCs must match. Because the PSF introduces a shift of the atomic lattice that is not a lattice translation vector, the Bloch wavefunctions of the two NCs do not share the same phase and, thus, are not able to couple. This observation is similar to the "bond-sign disorder" proposed by Delerue and co-workers.[106] This inhibited coupling appears to be an interesting consequence of PSF formation and is further supported by our electronic structure calculation of the "$\{11\bar{2}0\}$ Partial PSF" where we observe electron density across the perfect part of the interface and a lack of electron density along the part with the PSF (Figure S11). The ability of PSFs to still create confined states even in attached materials presents interesting possibilities for strongly coupled yet confined systems.

Determining Ideal Attachment Facets for Wurtzite CdSe.

One overarching goal of this paper was to rationally determine the ideal attachment facet for wurtzite CdSe NCs in the context of minimizing structural defects. As is evident, there is no attachment facet in wurtzite CdSe that leads to an easy removal pathway for all dislocations. This is in contrast to PbTe, and likely more generally, the rock salt lattice where {100} attachment provided fast dislocation removal kinetics compared to {110} attachment.[55] The CdSe case is more nuanced, and we must consider many aspects, including the shape-controlled synthesis prospects, coupling strength, potential dislocations formed, electronic consequences of those defects, and dislocation removal prospects**.**

One aspect that must be considered is the prospect of controllably preparing prismatic facet specific NCs. In this work, we were able to prepare comparable samples of CdSe terminated with both the $\{1\bar{1}00\}$ and $\{11\bar{2}0\}$ facets. Unfortunately, we were only able to achieve this control with large (~15 nm) NCs and we were unable to prepare sub-15 nm $\{11\bar{2}0\}$ terminated CdSe. For CdSe and most other interesting wurtzite semiconductor NCs, this is larger than the exciton Bohr radius in those materials. One big motivator for developing atomically coherent attachment of semiconductor NCs is the goal of producing "confined but connected" solids, where the quantum confined electronic states of the individual NCs are strongly coupled. Thus, we would need to start with small CdSe NCs to contribute to this endeavor and currently only $\{1\bar{1}00\}$ terminated CdSe NCs are available in small sizes. Furthermore, heterostructured NCs such as core shell CdSe/CdS also routinely display $\{1\bar{1}00\}$ surface faceting. We believe considerable synthetic breakthroughs will be needed to prepare small, strongly quantum confined, $\{11\bar{2}0\}$ terminated CdSe, heterostructured CdSe/CdS, or other wurtzite semiconductors. There is a strong case for pursuing connected wurtzite semiconductors on $\{1\bar{1}00\}$ facets.

Attachment on different facets may modulate the strength of coupling between neighboring NCs and is an important consideration if the goal is to prepare materials with delocalized electronic

states. The carrier densities shown in Figure 2 show that there is little qualitative difference in the carrier delocalization between the two attachment facets in the electron or hole states in both the noninteracting or interacting picture, suggesting that the attachment facet is not the most important factor in determining the electronic coupling. This finding can be understood by considering that the attachment on the $\{1\bar{1}00\}$ and $\{11\bar{2}0\}$ facets represent extending the electronic structure along different slices of the Brillouin zone in bulk CdSe.[107] Because carrier effective masses are predicted to modulate the resulting miniband structure in patterned electron gasses,[108] the differences in the electronic couplings should be dictated by the differences in the hole effective mass in the light hole band along $\Gamma \rightarrow$ K for the $\langle 1\bar{1}00\rangle$ direction and $\Gamma \rightarrow$ M for the $\langle 11\bar{2}0\rangle$ direction as the electron effective masses are the same in both directions ($m_e = 0.12m_0$).[109] In CdSe, the light hole effective masses are almost identical for the two directions ($m_{lh} = 0.18m_0$ for $\langle 1\bar{1}00\rangle$ and $m_{lh} = 0.16m_0$ for $\langle 11\bar{2}0\rangle$).[109] In more strongly confined systems, the heavy hole properties are likely more important since heavier quasiparticles are less sensitive to confinement effects[110,111] and, thus, will become the valence band edge state. In this case, the effective masses differ by less than a factor of two ($m_{hh} = 0.9m_0$ for $\langle 1\bar{1}00\rangle$ and $m_{hh} = 1.7m_0$ for $\langle 11\bar{2}0\rangle$),[109] potentially leading to small differences. Thus, this simple analysis is in agreement with our findings of similar electronic coupling for NC attachment on the $\{1\bar{1}00\}$ and $\{11\bar{2}0\}$ facets. A quantitative measure of the electronic coupling between the two attached NCs is the energy difference between the bonding and antibonding states of the lowest energy electron states. Our calculations found splittings of 4.5 meV for $\{1\bar{1}00\}$ attachment and 3.8 meV for $\{11\bar{2}0\}$ attachment. Due to these similar splittings and the predictions of a highly non-linear dependence of the coupling strength on the epitaxial connection area,[112] we believe facet dependent coupling is of secondary importance in materials with similar direction specific charge carrier effective masses.

As discussed in the first section, avoiding edge dislocations which require climb to be expelled from the interface would greatly expedite defect removal. Here we consider the merits of attaching wurtzite CdSe on the two prismatic facets in the context of extended defect formation and removal prospects. Attachment on both the $\{1\bar{1}00\}$ and $\{11\bar{2}0\}$ facets leads to the formation of $b = \frac{a}{3}\langle 11\bar{2}0\rangle$ edge dislocations with different relative orientations of the glide planes to the surface where they can be removed. $\{1\bar{1}00\}$ attachment leads to an unfavorable glide plane which requires climb of the dislocation for successful removal. $\{11\bar{2}0\}$ attachment leads to two scenarios, one with a favorable glide plane and one with an unfavorable glide plane. As expected, the "$\{11\bar{2}0\} \perp$ Edge" is able to quickly glide out of the material whereas the "$\{11\bar{2}0\} \parallel$ Edge" is forced to more slowly climb out of the material. Considering the low incidence of the "$\{11\bar{2}0\} \perp$ Edge", there is little difference in the edge dislocation removal, because unfavorable glide plane scenarios occur for both $\{1\bar{1}00\}$ and $\{11\bar{2}0\}$ attachment.

In the first section we identified that PSFs bound by a partial dislocation are easily removed while PSF's across the whole interface are stable. Considering the non-negligible electronic consequences of PSFs, they should be avoided if the desire is to prepare defect free materials. In the case of $\{11\bar{2}0\}$ attachment, there is a pathway to the formation of PSFs and partial PSFs at the interface of the particles (Figure 3 E, I). Whereas for attachment on the $\{1\bar{1}00\}$ we did not observe PSFs. For this reason, we believe $\{11\bar{2}0\}$ attachment is less favorable if the desire is to prepare

defect free interfaces between attached NCs since $\{1\bar{1}00\}$ attachment avoids the formation of PSFs.

Defects are only undesirable if they result in deleterious properties and in this case, we consider the electronic consequences of those defects. With regard to $b = \frac{a}{3}\langle 2\bar{1}\bar{1}0\rangle$ edge dislocations, which results in deep level hole traps (Figures 4E-H), attachment on either facet can lead to the formation of this edge dislocation with unfavorable removal geometries. Thus, either facet leads to undesirable electronic states coming from perfect edge dislocations. Defects such as PSFs and $b = \frac{a}{2}[\bar{1}011]$ partial dislocations, which both lead to mid-gap, shallow hole trap states (Figure 4A-D, and Figure S11) and deep hole traps in the latter case, make the $\{11\bar{2}0\}$ facet less appealing. This preference for attaching $\{1\bar{1}00\}$ faceted NCs to avoid PSFs is exacerbated in the case of perfect PSF's because they can't be removed and likely these defects will persist even after considerable thermal treatment. Considering that PSFs (and associated electronic consequences) and related defects only arise from $\{11\bar{2}0\}$ attachment, the $\{1\bar{1}00\}$ facet is more desirable for attachment when considering the electronic consequences of the dislocations.

Taken together, we believe that, if the goal is to prepare defect free materials, there are fewer negative consequences for attachment on the $\{1\bar{1}00\}$ facet. The specific advantages of the $\{1\bar{1}00\}$ facet are as follows: $\{1\bar{1}00\}$ terminated CdX materials are typically easier to synthesize and $\{1\bar{1}00\}$ attachment does not lead to PSF type defects. The other considerations such as coupling strength, other defect types, and removal are all relatively equal for the different facets. Our considerations are by no means comprehensive nor do the specifics necessarily hold for materials other than CdSe. Nonetheless, we hope to have presented guidelines and the thought process for designing defect free oriented attachment of NCs.

While there is considerable desire is to prepare defect free semiconductor solids from attaching NCs, in practice it may prove too difficult to sufficiently decrease the extended defect concentration. Instead we discuss devices which take advantage of the extended defect electronic levels. In one mode of operation, semiconductor photodetectors operate by trapping the minority carrier for a long time.[113,114] For example, in the past, our group has used spatially controlled doping of CdTe grain boundaries with Cl to trap holes at the grain interior and transfer the electrons to the highly conductive grain boundary.[46] The percolative network of grain boundaries allowed for detection of the photogenerated current. Impressively, these materials exhibited a specific detectivity of $5\text{x}10^{17}$ Jones, orders of magnitude higher than single crystal detectors. To see how this strategy could be implemented with epitaxially attached NCs, consider the results of the electronic structure calculations (Figure 4). In CdSe, edge dislocations lead to the trapping of holes while only minimally effecting the unbound (noninteracting) electron states. This could allow for similar minority carrier trap mediated photoconductivity, however now the un-trapped carrier resides in a single crystal domain of covalently attached NCs, and potentially will be much more mobile than percolative grain boundary conductivity.

Superlattice assembly tolerances and ideal geometries for atomic attachment.

While the attachment of individual NCs provides a step towards extended solids, attachment of multiple NCs considerably complicates many of the considerations. One such complication is that a single imperfect attachment leads to orientational misalignment that can propagate disorder and lead to other imperfect attachment events. Herein, we discuss the origin of dislocations in attached

NC arrays and angular alignment tolerances to avoid undesirable multiple dislocation events. The superlattice geometry, in particular weather it tiles all space, is a final consideration for preparing defect free quantum dot solids.

The traditional view of imperfect oriented attachment invokes a surface step getting trapped at the interface between two particles.[32] However in our samples, and in many other examples,[28,115–117] the particles are pre-assembled as crystallographically aligned NCs (albeit with some mistilt) with organic ligands separating the inorganic cores, followed by ligand removal to induce attachment. An alternative mechanism for edge dislocation formation, is that particles with pristine facets can be locked with some mistilt between them enforced by the local arrangement of NCs or size inhomogeneity. When they attach with a mistilt, initially an atomic bridge can form between the particles,[118] and the energy of the interface between the tilted particles is minimized by forming a dislocation through different amounts of atom migration to the opposite sides of the bridge between the misoriented particles. In this picture, pre-assembly of NCs with the smallest amount of mistilt possible will be necessary for defect free attachment. Alternatively, NCs with surface steps would likely cause angular distributions among assembled particles. Observation of the attachment process *in-situ* where the initial configuration of the NCs and their surface geometry is known will likely be needed to answer this question. If the dislocations in these attached materials result from the traditional imperfect oriented attachment view, development of step-edge free NC synthesis methods will be needed, however if the angular misalignment of otherwise pristine surfaces leads to dislocation formation, better controlled self-assembly will be needed to avoid misoriented particles.

Regardless of the origin of the mistilt between the particles, Equation 1 and Figure 7B provide a simple picture for the angular tolerance needed to avoid multiple dislocations at interfaces. An important takeaway from this plot is that the larger the particles become, the more stringent the mistilt tolerance becomes to avoid multiple dislocations which are considerably more difficult to remove. On the other hand, when assembling NCs, smaller particles would be expected to have more rotational disorder since they are less faceted and especially with the ligand shell would interact more like isotropic spheres. Studies of the rotational disorder in NC assemblies have been done using synchrotron x-ray scattering techniques and they have determined many factors that dictate the quality of the NC assembly.[5] These studies have mostly focused on determining the fraction of NCs aligned, not on the disorder of those that are aligned. Further ensemble angular alignment may not be the best measure for NC attachment, since only the misorientation between neighboring particles is important in determining attachment success. Despite unresolved questions regarding the origin or misorientation and the subsequent dislocations, we believe the angular alignment of the NCs can provide an indicator for success of atomic attachment of NCs.

Finally, we will consider the superlattice geometry and its importance in designing quantum dot solids. In this work, we explored the attachment of a close packed system of NCs that tiled all space. One observation was that interface defects between two particles migrated to the node where three particle edges met. Once there, the "node" defect density was not lowered even with thermal annealing at 440° C (Figure 6K). For an edge dislocation to be successfully removed, it must move to a free surface where it can be annihilated, or react with a dislocation with the opposite sense, the latter of which is unlikely. Thus, developing a geometry of attached NCs such that each NC interface is nearby a free surface will facilitate complete defect removal. One dimensional

chains[119–121] represent a scenario where the attachment interface always has a free surface for dislocations to anneal to. An example of an open 2D array of atomically attached NCs are the honeycomb lattices prepared by Vanmaekelbergh and co-workers.[115,122] In these honeycomb lattices, the necks between particles are surrounded on all sides by free surface where defects can anneal to. In the case of attachment of wurtzite CdSe, the hexagonal close packed layers do not afford this openness. Perhaps the co-assembly of CdSe NCs with a filler, such as a polymer micelle, would allow for the formation of honeycomb or other open lattice tilings that provide free surfaces throughout the entire assembly to serve as extended defects annihilation sites.

General insights related to atomically coherent attachment of inorganic materials.

We now discuss a few general implications for oriented attachment of inorganic materials based on our careful studies on the attachment of wurtzite CdSe on the prismatic facets. First, we discuss how our work relates to GaN epitaxial growth and single crystal h-BN growth. Next, we consider the possibility of predicting dislocation character resulting from atomic attachment for arbitrary materials. Finally, we propose similar projections for planar defect engineering from NC attachment. Altogether, we hope to inspire many routes to engineering defect (free) materials.

There are many similarities between oriented attachment of wurtzite CdSe and epitaxial growth of GaN and other hexagonal materials. Due to the lattice mismatch between GaN and the typical substrates used for growth, initial films often form Stranski–Krastanov islands of GaN which subsequently grow together and merge.[123–125] Small mistilts between the islands lead to low angle tilt boundaries when the islands fuse and, subsequently, many $b = \frac{1}{3}\langle 11\bar{2}0\rangle$ edge dislocations are formed.[125,126] This has many similarities to the preparation of CdSe NC solids where the pre-assembled NCs are misoriented by a small amount (Figure S4B shows an electron diffraction pattern of attached CdSe with peak shapes characteristic of mosaicity). In this respect, it is unsurprising that we observe many of the same dislocations when attaching wurtzite CdSe NCs as are seen when growing GaN along the [0001]. In another GaN example, steps on the SiC substrate surface can cause unit displacements along the [0001] direction between neighboring islands, leading to the formation of PSFs in GaN epitaxial layers.[91,92] In the case of NC attachment, random displacements along the [0001] direction are likely due to differences in NC ligand thickness, steps on the graphene support, or different thickness NCs.

Recently, there have been several reports of wafer scale growth of single crystal graphene and hexagonal boron nitride where island fusion is the observed growth mechanism.[127,128] In the case of hexagonal boron nitride, researchers used a liquid gold subphase where small single layer hexagonal boron nitride grains initially formed, and subsequently self-oriented and fused into wafer scale single crystals.[128] While the attachment facet was not explicitly determined, it will likely have a large impact on defect formation in these materials. Taken together, there are considerable similarities in growth and defect formation between the above discussed materials systems and the fields likely can learn from each other as they pursue their mutual goal of producing high quality materials by attaching nanoscale building blocks to each other.

Next, we consider if it is possible to predict the dislocation character based on the known surface steps that are present for a given facet. In Figure 3, we notice the step vector describing the type of surface step edge (yellow arrows Figures 3A,I,P) corresponds exactly with Burgers vector of the perfect edge dislocation (Figures 3B,M,Q). Upon reflection, this is the reverse process of an edge dislocation being expelled from a material, which leads to a step edge with the same

magnitude as the Burgers vector. With this insight, it should be possible to predict the glide plane of a dislocation that may result if the common surface steps are known for a given crystal structure and attachment facet. This surface step and Burgers vector relationship is further supported by our previous work on PbTe, where a $\frac{1}{2}[110]$ surface step on a (100) facet lead to a $b = \frac{1}{2}[110]$ edge dislocation with a favorable glide plane.[55] Whereas a $\frac{1}{2}[110]$ surface step on a (110) leads to a $b = \frac{1}{2}[110]$ edge dislocation with an unfavorable glide plane. Details of this are shown in Figure S12. The consistency of this observation in both the rock salt and wurtzite structure suggests it may be useful in predicting ideal attachment facets for many materials. Furthermore, predictions of the most probable surface step edges are possible using a variety of methods (HRTEM, geometric considerations, or theory) and can aid in attachment facet decision making.

Finally, we consider the possibility of engineering planar defects during NC attachment. We noticed that attachment on $\{11\bar{2}0\}$ facets lead to PSFs which reside in the $\{11\bar{2}0\}$ planes whereas no PSFs formed during attachment on $\{1\bar{1}00\}$ facets. In considering the generality of this observation, we can learn from the oriented attachment of $CsPbBr_3$ NCs on {100} facets into extended solids.[129–132] In this case, researchers have observed the formation of {100} antiphase boundaries, also known as Ruddlesden–Popper planar faults, from the attachment of $CsPbBr_3$ NCs on {100} facets. Based on these considerations, avoiding attachment on facets for which a planar defect in the material can reside may avoid the formation of those defects in attached NC solids. Conversely, if the planar defects have desirable properties, attachment facet choice could be used to prepare materials with engineered defects. PSFs in wurtzite CdSe attached on $\{11\bar{2}0\}$ facets and antiphase boundaries in halide perovskites attached on {100} facets provide two supporting examples.

Conclusions

In this work, we explored many considerations for atomically attaching wurtzite CdSe NCs on $\{1\bar{1}00\}$ and $\{11\bar{2}0\}$ facets within the context of preparing defect free solids. We found that attachment on both $\{1\bar{1}00\}$ and $\{11\bar{2}0\}$ facets can lead to crystallographically coherent attachment and delocalized electron and hole states with similar electronic coupling strengths. In cases of imperfect attachment on $\{1\bar{1}00\}$ facets, we observed the formation of $b = \frac{a}{3}[2\bar{1}\bar{1}0]$ edge dislocations which lead to localized mid-gap hole traps. These dislocations can be annealed out of the interface albeit requiring dislocation climb. In the case of $\{11\bar{2}0\}$ facet attachment, we observed four distinct dislocation types resulting from imperfect attachment. Specifically, we found PSF's across the entire interface that are very difficult to remove and are predicted to lead to shallow hole trap states. We also observed $b = \frac{a}{2}[\bar{1}011]$ partial dislocations terminated by a PSF that likely lead to deep hole traps but were easy to remove. Finally, for $\{11\bar{2}0\}$ facet attachment, we observed two different $b = \frac{a}{3}\langle 2\bar{1}\bar{1}0\rangle$ edge dislocation scenarios, one which had a favorable glide plane for removal and the other which had an unfavorable glide plane for removal. Regarding some aspects, the two facets have comparable (dis)advantages: in the case of CdSe, there is no obvious difference in the electronic coupling strength of the two facets, and they both lead to the formation of $b = \frac{a}{3}\langle 2\bar{1}\bar{1}0\rangle$ edge dislocations and their associated deep hole traps. That

being said, after careful consideration, we believe attaching wurtzite CdSe NCs on the $\{1\bar{1}00\}$ facet is better for several reasons including: greater synthetic maturity for preparation of $\{1\bar{1}00\}$ terminated CdSe NCs, $\{1\bar{1}00\}$ attachment avoids PSF formation, and while not ideal, $b = \frac{a}{3}[2\bar{1}\bar{1}0]$ edge dislocations can be removed with annealing though a combination of dislocation glide and climb.

While there appears to be a path forward dealing with imperfect attachment resulting in single dislocations at interfaces, we elucidated that multiple dislocations, regardless of attachment facet, were unable to be removed even with considerable annealing. Thus, an imperative design principle is to avoid the formation of multiple dislocations. Considering defective interfaces between NCs as snapshots of low angle tilt boundaries, a simple analytical model provides guidelines for angular tolerances needed to avoid multiple dislocations. Based on observations of dislocations formed in PbTe[55] and CdSe, we suggest that careful considerations of the step edges on surfaces can be used to predict the character of the dislocations arising from imperfect oriented attachment. A similar consideration of planar defects in CdSe and $CsPbBr_3$ suggests a rational design principle to control planar defects from particle attachment. Taken together, we hope this work provides guidelines for engineering (or eliminating) defects in atomically coherent arrays of attached NCs.

Despite the immense desire to realize the intriguing theorized electronic properties predicted for arrays of atomically attached semiconductor NCs,[38,39,133] experimental realization of these materials lags considerably, having achieved delocalization lengths only on the order of tens of nanometers.[28] Thus, the pathways which lead to deleterious defects, identification of deleterious defects through both experimental and theoretical endeavors, and new strategies for defect free synthesis will need to be understood and developed to realize attached NC arrays of sufficient quality to realize these delocalized electronic properties. While noble, the tolerances for realizing delocalized carriers may be too tight, and rather NC attachment can be harnessed to engineer defect states which in and of themselves provide desirable properties. In this work, many similarities were observed between defective NC attachment and dislocations in bulk materials. Considering the similarities, the NC attachment community can be inspired by strategies in traditional semiconductor processing, such as dislocation free silicon growth and high quality GaN epitaxial growth, where defects have been engineered or eliminated to provide the desired functionality.

Materials and Methods

Materials. cadmium Oxide (CdO) 99.99% Aldrich; oleic acid 90% (OA) technical grade Aldrich; oleylamine (OAm) technical grade 70% Aldrich; octadecene 90% (ODE) technical grade Aldrich; n-trioctylphosphine 97% (TOP) Strem; methanol 99.5% extra dry Acros; cetyltrimethylammonium chloride (CTAC) >95% TCI; dioctyl ether (OE) 99% Aldrich; selenium 99.99% Strem; sodium selenide (Na_2Se) 99.5% Alfa Aesar; CVD graphene on copper 3−5 layer ACS materials; Quantifoil R1.2/1.3 300 mesh Au holey carbon SPI supplies; Ultrathin Carbon Film on Lacey Carbon Support Film, 300 mesh, Gold (1824G Ted Pella Inc.).

Nanocrystal Synthesis. Wurtzite CdSe NCs with $\{1\bar{1}00\}$ and $\{11\bar{2}0\}$ termination were synthesized based on heavily modified literature procedures.[72]

Zinc blende CdSe Seeds were prepared as follows: 8mmol CdO (1028 mg), 20mmol OA (6.4 ml), and 40 ml of ODE were loaded into a 100ml round bottom flask and degassed on a Schlenk line at 110 °C for 1 hour. The flask was filled with argon and heated to 210 °C to form a Cd-oleate complex. Meanwhile, in a glovebox, 4 mmol Se (316 mg), 3.32 g TOP, and 5.49 g ODE were stirred until all the Se dissolved, and then loaded into a syringe. The contents of the syringe were rapidly injected into the Cd-oleate solution at 210 °C and allowed to react for 20 min. The samples were cooled to room temperature and cleaned 2X in air by precipitating the NCs with ethanol and centrifuged at 8000rpm. The resulting pellet was dissolved in hexanes. Samples were transferred to a glovebox and stored in hexanes. The concentration of the NC solution was determined photometrically using known size dependent extinction coefficients.[134]

$\{1\bar{1}00\}$ Terminated Wurtzite CdSe: 400 µl of OA, 412 µl of OAm, 40 mg of CTAC, and 5 ml of octyl ether were loaded into a 25ml round bottom flask and degassed at 50 °C for 20 min. While still under vacuum, a hexanes solution of zb CdSe seeds were added to give a Cd:Cl ratio of 1:1 and the solution was degassed to remove the volatiles. The flask was refilled with argon and heated to 260 °C. After 10 min at 260 °C, a ~1.5 ml aliquot was removed and quenched in room temperature toluene. Samples were cleaned 2X in air by precipitating the NCs with acetone and centrifuged at 8000rpm. The resulting pellet was dissolved in hexanes. A final centrifugation of the sample in hexanes was performed to remove any insoluble material.

$\{11\bar{2}0\}$ Terminated Wurtzite CdSe: 400 µl of OA, 412 µl of OAm, 40 mg of CTAC, and 5 ml of octyl ether were loaded into a 25ml round bottom flask and degassed at 50 °C for 20 min. While still under vacuum, a hexanes solution of zb CdSe seeds were added to give a Cd:Cl ratio of 1:1 and the solution was degassed to remove the volatiles. The flask was refilled with argon and heated to 280 °C for 20 min. After 20 min, the reaction was quickly cooled to room temperature using a stream of air. Samples were cleaned 2X in air by precipitating the NCs with acetone and centrifuged at 8000rpm. The resulting pellet was dissolved in hexanes. A final centrifugation of the sample in hexanes was performed to remove any insoluble material.

Nanocrystal Attachment and TEM sample Preparation. All samples of attached NCs were prepared using gold TEM grids. In some cases, we used homemade Graphene-coated TEM grids which were prepared by direct transfer of 3−5 layer graphene onto holey quatifoil TEM grids.[135] In other cases, samples were prepared on ultrathin carbon supports (1824G Ted Pella Inc.). Dilute solutions of the desired NCs in toluene were drop cast on the TEM grid, and the large excess of solvent was wicked away, leaving a small droplet covering the TEM grid. The grid was covered with a watch glass and allowed to slowly dry. After several hours, the TEM grid was picked up using anti-capillary self-closing tweezers and carefully pumped into a nitrogen filled glovebox. The sample was then dipped in a solution of Na_2Se in anhydrous methanol (1.66 mg/ml) for 45 s followed by dipping in neat anhydrous methanol to remove excess Na_2Se. The sample was then placed in the glovebox antechamber and placed under vacuum to remove excess methanol. TEM samples were stored in air with no obvious degradation occurring over several months.

X-Ray Diffraction. To avoid orientation effects, the NCs were made into fine powders. Powders were prepared by depositing large amounts of the NCs from hexanes onto a glass slide, and allowed to dry, the film was then scraped off the glass slide with a clean razor blade onto a

⟨510⟩ oriented Si low background diffraction substrate. Diffraction patterns were collected on a Bruker Phaser D2 diffractometer with Cu kα source operated at 30 kV and 10 mA with a 160SSD detector. Diffraction patterns were collected from 20° to 60° 2θ with a step size of 0.02°, an integration time of 7s per step.

TEM imaging. TEM imaging was performed on a FEI Tecnai T20 S-TWIN TEM operating at 200 kV with a LaB6 filament. Images were taken near Scherzer focus, which resulted in dark atom contrast for this crystal thickness. Time series of TEM images were collected with a Gatan Orius SC200 using a custom digital micrograph script with full 2048 × 2048 pixel readout, at a nominal magnification of 195k×, resulting in a pixel resolution of 0.27 Å/pixel, an exposure time of .7s, and a readout time of 1.4 s, yielding a frame rate of 0.48 fps. Since the defect dynamics were beam initiated, care was taken to minimize electron dose prior to imaging. Searching was performed with a spread beam; then once a suitable defective nanoparticle was found, a custom Digital Micrograph script was used to condense the beam to reproducibly return to the same dose rate within a session for each movie acquisition.[96] We estimate a dose rate of~5000 $e^{-}/Å^{2}\cdot s$ was used for all data collected and a conversion value of 6.7 was used to convert CCD counts to electrons. For thermal annealing experiments ~150 HRTEM images of attached particles were first collected, then the sample was annealed in the TEM column (8.8×10^{-8} torr pressure) at 440°C for 15min in a Gatan model 628 crucible heating holder with an inconel furnace. The sample was then cooled back to room temperature and another ~150 HRTEM images were collected.

TEM image analysis. TEM image stacks were first drift corrected with subpixel accuracy using the image alignment tools in Gatan Digital Micrograph 3.0 (GMS 3.0) and alignment success was manually inspected. In some cases, the raw images were used for drift correction and in other cases, a Sobel or Hanning filter produced better alignment. For all FTs displayed and analyzed care was taken to avoid streaking artefacts that result from image edges. Briefly in GMS 3.0, a 2^{n} by 2^{n} pixel area of interest was cropped from the image and was subsequently multiplied by a 2D Hanning window followed by computing the FT. For visualization, the log of the modulus of the FT was saved and visualized in ImageJ using the "fire" lookup table to facilitate viewing. The position of edge dislocations were determined using the same strategy we used previously.[55] Prismatic stacking fault presence was determined by analyzing the streak intensity in the FT. First a Hanning filtered FT of a sub-area of each frame was computed, then a mask was used to select only the streak area, and a sum of the counts was computed. A Hanning filtered FT of the same size of a nearby sub-area from the same image series where a perfect crystal was observed was also computed. The same mask was used to determine the background intensity in the FT. To account for fluctuations in image quality with time, the FT streak intensity was normalized by the intensity of the $\{1\bar{1}00\}$ spots in the FT from the perfect crystal sub-area.

For heating experiment analysis, a custom automated Matlab routine was written to identify imperfections in the lattice which was used as an aide to manually identify dislocation density. First a Fourier transform of the image was calculated and the 6 spots corresponding to the $\{1\bar{1}00\}$ planes were automatically found to determine the rotation of the lattice in the image. Next the image was separately Fourier filtered by 3 different masks corresponding to the $(1\bar{1}00)$ $(10\bar{1}0)$ $(0\bar{1}10)$ planes. Each Fourier filtered image was then binarized and skeletonized then the endpoints

and branchpoints of the skeleton image were determined (these correspond to potential edge dislocations). Only branch and endpoints from image areas with inverse FT magnitude above a certain threshold were kept by the routine. Finally, the raw image, Fourier filtered images, and image overlaid with the potential dislocation positions were displayed side by side in a Matlab figure. In each image, the number of interfaces as well as the number of dislocations and PSFs were manually counted after careful inspection of each potential dislocation determined by the image analysis routine. The routine was written and tuned to be oversensitive to avoid missing any dislocations.

Computational Methods. Initial structures of the imperfectly attached NCs were generated by cutting from large crystal slabs which contained the desired dislocation. Slabs of wurtzite with the different dislocation structures were generated using the ATOMSK software.[136] Briefly, a wurtzite CdSe unit cell was generated in ATOMSK using bulk lattice constants. Next, the primitive unit cell was converted to an orthogonal unit cell with lattice vectors X, Y and Z along the $[11\bar{2}0]$, $[\bar{1}100]$ and $[0001]$ directions in wurtzite, respectively, and a supercell of sufficient size was generated. The edge dislocations were introduced into this slab using isotropic elasticity theory using a Poisson ratio of 0.26. For the $b = \frac{a}{3}[2\bar{1}\bar{1}0]$ edge dislocations, an edge dislocation in the center of the supercell with a sense along the Z direction of the supercell and a displacement of 4.30 Å along the X direction was introduced into the supercell. The exact center of the dislocation was optimized to prevent it from occurring on an atomic position to avoid non-physical displacements. For the $b = \frac{a}{2}[\bar{1}011]$ partial dislocations, first, an edge dislocation in the center of the supercell with a sense along the Z direction of the supercell and a displacement of 2.15 Å along the X direction was introduced into the supercell. Next, a screw dislocation with a displacement of 3.51 Å along the Z direction was introduced. For the prismatic stacking faults, a displacement of 3.73 Å in the Y direction and 3.51 Å in the Z direction was introduced into the supercell.

Imperfectly attached NCs were cut from these slabs according to the following procedure. Two spherical masks were created with their centers equidistant from the dislocation core, and the atoms outside of these masks were removed. The intersection of the two spheres determined the particle interface and contained the relevant dislocation. The individual spheres were approximately 6.5 nm in diameter. The size and intersection of the NCs were tuned such that all the attached NC structures had approximately the same number of atoms and atoms at their interface. We used the same procedure to create the perfectly attached NCs.

We then performed molecular dynamics based geometry minimization of the NCs *via* the conjugate gradient algorithm implemented in LAMMPS[137] using previously developed Stillinger-Weber interaction potentials for CdSe.[82] To obtain the final configuration for which we ran the electronic structure calculations, the outermost layer of atoms was removed and the subsequent monolayer was replaced by ligand potentials representing the passivation layer, where each Se (Cd) atom was replaced by a ligand potential for Cd (Se).[138] For the imperfectly attached NCs, care was taken to ensure that the defect site was not disrupted by this passivation procedure. Specifically, we did not passivate the interior atoms of the defects, but we did passivate the atoms on the top and bottom of the defect site. An atom was categorized as interior if all positions along

the surface of a sphere centered at the atom with a radius of ~3.5 Å were within ~3 Å of at least one atom or if the atom had four bonds.

Electronic structure calculations were performed using the semi-empirical pseudopotential method.[81] The filter-diagonalization technique[83,84] was used to find the quasiparticle states near the band-edge. These quasiparticle states were then used to produce carrier density plots and, separately, as input to the Bethe-Salpeter equation to obtain the correlated electron-hole (i.e. excitonic) states.[85] The Bethe-Salpeter equation was solved within the static dielectric approximation ($\varepsilon = 5$).

Associated Content

Supporting Information

Figure S1-Figure S12

Video S1: HRTEM movie of imperfectly attached $\{1\bar{1}00\}$ terminated CdSe NCs with a $b = \frac{a}{3}[2\bar{1}\bar{1}0]$ edge dislocation.

Video S2: HRTEM movie of imperfectly attached $\{11\bar{2}0\}$ terminated CdSe NCs with a PSF across the entire interface.

Video S3: HRTEM movie of imperfectly attached $\{11\bar{2}0\}$ terminated CdSe NCs with a PSF across part of the interface which is terminated with a partial dislocation.

Video S4: HRTEM movie of imperfectly attached $\{11\bar{2}0\}$ terminated CdSe NCs with a $b = \frac{a}{3}[2\bar{1}\bar{1}0]$ edge dislocation with a perpendicular glide plane for removal.

Video S5: HRTEM movie of imperfectly attached $\{11\bar{2}0\}$ terminated CdSe NCs with a $b = \frac{a}{3}[11\bar{2}0]$ edge dislocation with a parallel glide plane for removal.

Video S6: HRTEM movie of imperfectly attached $\{11\bar{2}0\}$ terminated CdSe NCs with two edge dislocations

Video S7: HRTEM movie of imperfectly attached $\{1\bar{1}00\}$ terminated CdSe NCs with two edge dislocations

Author Information

Corresponding Author

*Email: paul.alivisatos@berkeley.edu

Notes

The authors declare no competing financial interest.

Acknowledgements

The experimental aspects of this work (TEM, image analysis, and analytical models) were supported by the National Science Foundation, Division of Materials Research (DMR), under award number DMR-1808151. Theoretical aspects of this work were synergistically supported by the U.S. Department of Energy, Office of Science, Office of Basic Energy Sciences, Materials Sciences and Engineering Division, under Contract No. DE- AC02-05-CH11231, within the Physical Chemistry of Inorganic Nanostructures Program (KC3103). J.C.O gratefully acknowledges the support of the Chevron-UC Berkeley Graduate Student Fellowship. The authors would like to thank Arunima Balan and Matthew Hauwiller for useful discussions.

References

(1) Boles, M.; Engel, M.; Talapin, D. V. Self-Assembly of Colloidal Nanocrystals: From Intricate Structures to Functional Materials. *Chem. Rev.* **2016**, *116*, 11220–11289.

(2) Boles, M. A.; Talapin, D. V. Many-Body Effects in Nanocrystal Superlattices: Departure from Sphere Packing Explains Stability of Binary Phases. *J. Am. Chem. Soc.* **2015**, *137*, 4494–4502.

(3) Lin, X. M.; Sorensen, C. M.; Klabunde, K. J. Ligand-Induced Gold Nanocrystal Superlattice Formation in Colloidal Solution. *Chem. Mater.* **1999**, *11*, 198–202.

(4) Castelli, A.; de Graaf, J.; Marras, S.; Brescia, R.; Goldoni, L.; Manna, L.; Arciniegas, M. P. Understanding and Tailoring Ligand Interactions in the Self-Assembly of Branched Colloidal Nanocrystals into Planar Superlattices. *Nat. Commun.* **2018**, *9*, 1141.

(5) Weidman, M. C.; Nguyen, Q.; Smilgies, D. M.; Tisdale, W. A. Impact of Size Dispersity, Ligand Coverage, and Ligand Length on the Structure of PbS Nanocrystal Superlattices. *Chem. Mater.* **2018**, *30*, 807–816.

(6) Choi, J. J.; Bealing, C. R.; Bian, K.; Hughes, K. J.; Zhang, W.; Smilgies, D. M.; Hennig, R. G.; Engstrom, J. R.; Hanrath, T. Controlling Nanocrystal Superlattice Symmetry and Shape-Anisotropic Interactions through Variable Ligand Surface Coverage. *J. Am. Chem. Soc.* **2011**, *133*, 3131–3138.

(7) Quan, Z.; Xu, H.; Wang, C.; Wen, X.; Wang, Y.; Zhu, J.; Li, R.; Sheehan, C. J.; Wang, Z.; Smilgies, D. M.; et al. Solvent-Mediated Self-Assembly of Nanocube Superlattices. *J. Am. Chem. Soc.* **2014**, *136*, 1352–1359.

(8) Shevchenko, E. V.; Talapin, D. V.; Murray, C. B.; O'Brien, S. Structural Characterization of Self-Assembled Multifunctional Binary Nanoparticle Superlattices. *J. Am. Chem. Soc.* **2006**, *128*, 3620–3637.

(9) Diroll, B. T.; Greybush, N. J.; Kagan, C. R.; Murray, C. B. Smectic Nanorod Superlattices Assembled on Liquid Subphases: Structure, Orientation, Defects, and Optical Polarization. *Chem. Mater.* **2015**, *27*, 2998–3008.

(10) Ye, X.; Zhu, C.; Ercius, P.; Raja, S. N.; He, B.; Jones, M. R.; Hauwiller, M. R.; Liu, Y.; Xu, T.; Alivisatos, A. P. Structural Diversity in Binary Superlattices Self-Assembled from Polymer-Grafted Nanocrystals. *Nat. Commun.* **2015**, *6*, 10052.

(11) Rabani, E.; Reichman, D. R.; Geissler, P. L.; Brus, L. E. Drying-Mediated Self-Assembly

of Nanoparticles. *Nature* **2003**, *426*, 271–274.

(12) Lin, X. M.; Jaeger, H. M.; Sorensen, C. M.; Klabunde, K. J. Formation of Long-Range-Ordered Nanocrystal Superlattices on Silicon Nitride Substrates. *J. Phys. Chem. B* **2001**, *105*, 3353–3357.

(13) Talapin, D. V.; Shevchenko, E. V.; Kornowski, A.; Gaponik, N.; Haase, M.; Rogach, A. L.; Weller, H. A New Approach to Crystallization of CdSe Nanoparticles into Ordered Three-Dimensional Superlattices. *Adv. Mater.* **2001**, *13*, 1868.

(14) Urban, J. J.; Talapin, D. V.; Shevchenko, E. V.; Kagan, C. R.; Murray, C. B. Synergism in Binary Nanocrystal Superlattices Leads to Enhanced P-Type Conductivity in Self-Assembled PbTe/Ag2Te Thin Films. *Nat. Mater.* **2007**, *6*, 115–121.

(15) Cargnello, M.; Johnston-Peck, A. C.; Diroll, B. T.; Wong, E.; Datta, B.; Damodhar, D.; Doan-Nguyen, V. V. T.; Herzing, A. a; Kagan, C. R.; Murray, C. B. Substitutional Doping in Nanocrystal Superlattices. *Nature* **2015**, *524*, 450–453.

(16) Ye, X.; Chen, J.; Eric Irrgang, M.; Engel, M.; Dong, A.; Glotzer, S. C.; Murray, C. B. Quasicrystalline Nanocrystal Superlattice with Partial Matching Rules. *Nat. Mater.* **2017**, *16*, 214–219.

(17) Talapin, D. V.; Shevchenko, E. V.; Bodnarchuk, M. I.; Ye, X.; Chen, J.; Murray, C. B. Quasicrystalline Order in Self-Assembled Binary Nanoparticle Superlattices. *Nature* **2009**, *461*, 964–967.

(18) Nagaoka, Y.; Zhu, H.; Eggert, D.; Chen, O. Single-Component Quasicrystalline Nanocrystal Superlattices through Flexible Polygon Tiling Rule. *Science* **2018**, *362*, 1396–1400.

(19) Weidman, M. C.; Smilgies, D.; Tisdale, W. A. Kinetics of the Self-Assembly of Nanocrystal Superlattices Measured by Real-Time in Situ X-Ray Scattering. *Nat. Mater.* **2016**, *15*, 775–782.

(20) Kovalenko, M. V.; Bodnarchuk, M. I.; Talapin, D. V. Nanocrystal Superlattices with Thermally Degradable Hybrid Inorganic-Organic Capping Ligands. *J. Am. Chem. Soc.* **2010**, *132*, 15124–15126.

(21) Dong, A.; Jiao, Y.; Milliron, D. J. Electronically Coupled Nanocrystal Superlattice Films by in Situ Ligand Exchange at the Liquid-Air Interface. *ACS Nano* **2013**, *7*, 10978–10984.

(22) Luther, J. M.; Law, M.; Song, Q.; Perkins, C. L.; Beard, M. C.; Nozik, A. J. Structural, Optical, and Electrical Properties of Self-Assembled Films of PbSe Nanocrystals Treated with 1,2-Ethanedithiol. *ACS Nano* **2008**, *2*, 271–280.

(23) Zarghami, M. H.; Liu, Y.; Gibbs, M.; Gebremichael, E.; Webster, C.; Law, M. P-Type PbSe and PbS Quantum Dot Solids Prepared with Short-Chain Acids and Diacids. *ACS Nano* **2010**, *4*, 2475–2485.

(24) Sharma, R.; Sawvel, A. M.; Barton, B.; Dong, A.; Buonsanti, R.; Llordes, A.; Schaible, E.; Axnanda, S.; Liu, Z.; Urban, J. J.; et al. Nanocrystal Superlattice Embedded within an Inorganic Semiconducting Matrix by in Situ Ligand Exchange: Fabrication and

Morphology. *Chem. Mater.* **2015**, *27*, 2755–2758.

(25) Lee, J.-S.; Kovalenko, M. V; Huang, J.; Chung, D. S.; Talapin, D. V. Band-like Transport, High Electron Mobility and High Photoconductivity in All-Inorganic Nanocrystal Arrays. *Nat. Nanotechnol.* **2011**, *6*, 348–352.

(26) Kovalenko, M. V; Schaller, R. D.; Jarzab, D.; Loi, M. a; Talapin, D. V. Inorganically Functionalized PbS-CdS Colloidal Nanocrystals: Integration into Amorphous Chalcogenide Glass and Luminescent Properties. *J. Am. Chem. Soc.* **2012**, *134*, 2457–2460.

(27) O'Regan, B.; Grätzel, M. A Low-Cost, High-Efficiency Solar Cell Based on Dye-Sensitized Colloidal TiO2 Films. *Nature* **1991**, *353*, 737–740.

(28) Whitham, K.; Yang, J.; Savitzky, B. H.; Kourkoutis, L. F.; Wise, F.; Hanrath, T. Charge Transport and Localization in Atomically Coherent Quantum Dot Solids. *Nat. Mater.* **2016**, *15*, 557–563.

(29) Walravens, W.; De Roo, J.; Drijvers, E.; Ten Brinck, S.; Solano, E.; Dendooven, J.; Detavernier, C.; Infante, I.; Hens, Z. Chemically Triggered Formation of Two-Dimensional Epitaxial Quantum Dot Superlattices. *ACS Nano* **2016**, *10*, 6861–6870.

(30) Sandeep, C. S. S.; Azpiroz, J. M.; Evers, W. H.; Boehme, S. C.; Moreels, I.; Kinge, S.; Siebbeles, L. D. a; Infante, I.; Houtepen, A. J. Epitaxially Connected PbSe Quantum-Dot Films: Controlled Neck Formation and Optoelectronic Properties. *ACS Nano* **2014**, *8*, 11499–11511.

(31) Evers, W. H.; Schins, J. M.; Aerts, M.; Kulkarni, A.; Capiod, P.; Berthe, M.; Grandidier, B.; Delerue, C.; Zant, H. S. J. Van Der; Overbeek, C. Van; et al. High Charge Mobility in Two-Dimensional Percolative Networks of PbSe Quantum Dots Connected by Atomic Bonds. *Nat. Commun.* **2015**, *6*, 1–8.

(32) Penn, R. L.; Banfield, J. F. Imperfect Oriented Attachment: Dislocation Generation in Defect-Free Nanocrystals. *Science* **1998**, *281*, 969–971.

(33) Tsai, M. H.; Chen, S. Y.; Shen, P. Imperfect Oriented Attachment: Accretion and Defect Generation of Nanosize Rutile Condensates. *Nano Lett.* **2004**, *4*, 1197–1201.

(34) Evers, W. H.; Goris, B.; Bals, S.; Casavola, M.; De Graaf, J.; Roij, R. Van; Dijkstra, M.; Vanmaekelbergh, D. Low-Dimensional Semiconductor Superlattices Formed by Geometric Control over Nanocrystal Attachment. *Nano Lett.* **2013**, *13*, 2317–2323.

(35) Queisser, H. J.; Haller, E. E. Defects in Semiconductors: Some Fatal, Some Vital. *Science* **1998**, *281*, 945–950.

(36) Sun, C.; Paulauskas, T.; Sen, F. G.; Lian, G.; Wang, J.; Buurma, C.; Chan, M. K. Y.; Klie, R. F.; Kim, M. J. Atomic and Electronic Structure of Lomer Dislocations at CdTe Bicrystal Interface. *Sci. Rep.* **2016**, *6*, 27009.

(37) Yang, J.; Wise, F. W. Effects of Disorder on Electronic Properties of Nanocrystal Assemblies. *J. Phys. Chem. C* **2015**, *119*, 3338–3347.

(38) Beugeling, W.; Kalesaki, E.; Delerue, C.; Niquet, Y.-M.; Vanmaekelbergh, D.; Morais Smith, C. Topological States in Multi-Orbital HgTe Honeycomb Lattices. *Nat. Commun.* **2015**, *6*, 6316.

(39) Kalesaki, E.; Delerue, C.; Morais Smith, C.; Beugeling, W.; Allan, G.; Vanmaekelbergh, D. Dirac Cones, Topological Edge States, and Nontrivial Flat Bands in Two-Dimensional Semiconductors with a Honeycomb Nanogeometry. *Phys. Rev. X* **2014**, *4*, 1–12.

(40) Holt, D. B.; Yacobi, B. G. *Extended Defects in Semiconductors*; Cambridge University Press, 2007.

(41) Fisher, G.; Seacrist, M. R.; Standley, R. W. Silicon Crystal Growth and Wafer Technologies. *Proc. IEEE* **2012**, *100*, 1454–1474.

(42) Dash, W. C. Growth of Silicon Crystals Free from Dislocations. *J. Appl. Phys.* **1959**, *30*, 459–474.

(43) Rudolf de Kock, A. J. Characterization and Elimination of Defects in Silicon. In *Treusch J. (eds) Festkörperprobleme 16. Advances in Solid State Physics, vol 16.*; 1976; pp 179–193.

(44) Hurle, D. T. J.; Rudolph, P. A Brief History of Defect Formation, Segregation, Faceting, and Twinning in Melt-Grown Semiconductors. *J. Cryst. Growth* **2004**, *264*, 550–564.

(45) Hanifi, D. A.; Bronstein, N. D.; Koscher, B. A.; Nett, Z.; Swabeck, J. K.; Takano, K.; Schwartzberg, A. M.; Maserati, L.; Vandewal, K.; van de Burgt, Y.; et al. Redefining Near-Unity Luminescence in Quantum Dots with Photothermal Threshold Quantum Yield. *Science* **2019**, *363*, 1199–1202.

(46) Zhang, Y.; Hellebusch, D. J.; Bronstein, N. D.; Ko, C.; Ogletree, D. F.; Salmeron, M.; Alivisatos, A. P. Ultrasensitive Photodetectors Exploiting Electrostatic Trapping and Percolation Transport. *Nat. Commun.* **2016**, *7*, 11924.

(47) Norman, Z. M.; Anderson, N. C.; Owen, J. S. Electrical Transport and Grain Growth in Solution-Cast, Chloride-Terminated Cadmium Selenide Nanocrystal Thin Films. *ACS Nano* **2014**, *8*, 7513–7521.

(48) Crisp, R. W.; Panthani, M. G.; Rance, W. L.; Duenow, J. N.; Parilla, P. A.; Callahan, R.; Dabney, M. S.; Berry, J. J.; Talapin, D. V.; Luther, J. M. Nanocrystal Grain Growth and Device Architectures for High-Efficiency CdTe Ink-Based Photovoltaics. *ACS Nano* **2014**, *8*, 9063–9072.

(49) Zhang, H.; Kurley, J. M.; Russell, J. C.; Jang, J.; Talapin, D. V. Solution-Processed, Ultrathin Solar Cells from CdCl3--Capped CdTe Nanocrystals: The Multiple Roles of CdCl3-Ligands. *J. Am. Chem. Soc.* **2016**, *138*, 7464–7467.

(50) Pennycook, S. J.; Al-Jassim, M.; Poplawsky, J.; Yin, W.; Pennycook, T. J.; Li, C.; Haigh, S. J.; Wu, Y.; Paudel, N.; Oxley, M. P.; et al. Grain-Boundary-Enhanced Carrier Collection in CdTe Solar Cells. *Phys. Rev. Lett.* **2014**, *112*, 1–5.

(51) Dick, K. A.; Thelander, C.; Samuelson, L.; Caroff, P. Crystal Phase Engineering in Single InAs Nanowires. *Nano Lett.* **2010**, *10*, 3494–3499.

(52) Trägårdh, J.; Capasso, F.; Wagner, J. B.; Bao, J.; Samuelson, L.; Mårtensson, T.; Bell, D. C. Optical Properties of Rotationally Twinned InP Nanowire Heterostructures. *Nano Lett.* **2008**, *8*, 836–841.

(53) Vlieg, E.; Feiner, L.-F.; Algra, R. E.; Bakkers, E. P. A. M.; Immink, G.; Verheijen, M. A.; Borgström, M. T.; van Enckevort, W. J. P. Twinning Superlattices in Indium Phosphide Nanowires. *Nature* **2008**, *456*, 369–372.

(54) Caroff, P.; Dick, K. A.; Johansson, J.; Messing, M. E.; Deppert, K.; Samuelson, L. Controlled Polytypic and Twin-Plane Superlattices in III-V Nanowires. *Nat. Nanotechnol.* **2009**, *4*, 50–55.

(55) Ondry, J. C.; Hauwiller, M. R.; Alivisatos, A. P. Dynamics and Removal Pathway of Edge Dislocations in Imperfectly Attached PbTe Nanocrystal Pairs; Towards Design Rules for Oriented Attachment. *ACS Nano* **2018**, *12*, 3178–3189.

(56) Peng, X.; Manna, L.; Yang, W.; Wickham, J.; Scher, E.; Kadavanich, A.; Alivisatos, A. P. Shape Control of CdSe Nanocrystals. *Nature* **2000**, *404*, 59–61.

(57) Chen, O.; Zhao, J.; Chauhan, V. P.; Cui, J.; Wong, C.; Harris, D. K.; Wei, H.; Han, H.-S.; Fukumura, D.; Jain, R. K.; et al. Compact High-Quality CdSe–CdS Core–shell Nanocrystals with Narrow Emission Linewidths and Suppressed Blinking. *Nat. Mater.* **2013**, *12*, 445–451.

(58) Sercel, P. C.; Efros, A. L. Band-Edge Exciton in CdSe and Other II-VI and III-V Compound Semiconductor Nanocrystals - Revisited. *Nano Lett.* **2018**, *18*, 4061–4068.

(59) Osipiyan, Y. A.; Smirnova, I. S. Perfect Dislocations in the Wurtzite Lattice. *Phys. Status Solidi* **1968**, *30*, 19–29.

(60) Osipyan, Y. A.; Smirnova, I. S. Partial Dislocations in the Wurtzite Lattice. *J. Phys. Chem. Solids* **1971**, *32*, 1521–1530.

(61) Blank, H.; Delavignette, P.; Amelinckx, S. Dislocations and Wide Stacking Faults in Wurtzite-Type Crystals: Zinc Sulphide and Aluminium Nitride. *Phys. Stat. Sol.* **1962**, *2*, 1660–1669.

(62) Vermaut, P.; Nouet, G.; Ruterana, P. Observation of Two Atomic Configurations for the {12$\bar{1}$0} Stacking Fault in Wurtzite (Ga, Al) Nitrides. *Appl. Phys. Lett.* **1999**, *74*, 694–696.

(63) Northrup, J. E. Shallow Electronic States Induced by Prismatic Stacking Faults in AlN and GaN. *Appl. Phys. Lett.* **2005**, *86*, 1–3.

(64) Corfdir, P.; Lefebvre, P.; Levrat, J.; Dussaigne, A.; Ganìre, J. D.; Martin, D.; Ristić, J.; Zhu, T.; Grandjean, N.; Deveaud-PĺdranB. Exciton Localization on Basal Stacking Faults in a -Plane Epitaxial Lateral Overgrown GaN Grown by Hydride Vapor Phase Epitaxy. *J. Appl. Phys.* **2009**, *105*.

(65) Takeuchi, S.; Suzuki, K.; Maeda, K.; Iwanaga, H. Stacking-Fault Energy of II-VI Compounds. *Philos. Mag. A* **1985**, *50*, 171–178.

(66) Labat, S.; Richard, M. I.; Dupraz, M.; Gailhanou, M.; Beutier, G.; Verdier, M.;

Mastropietro, F.; Cornelius, T. W.; Schülli, T. U.; Eymery, J.; et al. Inversion Domain Boundaries in GaN Wires Revealed by Coherent Bragg Imaging. *ACS Nano* **2015**, *9*, 9210–9216.

(67) Shiang, J. J.; Kadavanich, A. V; Grubbs, R. K.; Alivisatos, A. P. Symmetry of Annealed Wurtzite CdSe Nanocrystals. Assignment to C3vpoint Group. *J. Phys. Chem.* **1995**, *99*, 17417–17422.

(68) Cassette, E.; Mahler, B.; Guigner, J. M.; Patriarche, G.; Dubertret, B.; Pons, T. Colloidal CdSe/CdS Dot-in-Plate Nanocrystals with 2D-Polarized Emission. *ACS Nano* **2012**, *6*, 6741–6750.

(69) Mcbride, J.; Treadway, J.; Feldman, L. C.; Pennycook, S. J.; Rosenthal, S. J. Structural Basis for Near Unity Quantum Yield Core / Shell Nanostructures. *Nano Lett.* **2006**, *6*, 1496–1501.

(70) Pennycook, T. J.; McBride, J. R.; Rosenthal, S. J.; Pennycook, S. J.; Pantelides, S. T. Dynamic Fluctuations in Ultrasmall Nanocrystals Induce White Light Emission. *Nano Lett.* **2012**, *12*, 3038–3042.

(71) Frank, F. C. On Miller–Bravais Indices and Four-Dimensional Vectors. *Acta Crystallogr.* **1965**, *18*, 862–866.

(72) Saruyama, M.; Kanehara, M.; Teranishi, T. Drastic Structural Transformation of Cadmium Chalcogenide Nanoparticles Using Chloride Ions and Surfactants. *J. Am. Chem. Soc.* **2010**, *132*, 3280–3282.

(73) Cheng, Y.; Wang, Y.; Bao, F.; Chen, D. Shape Control of Monodisperse CdS Nanocrystals: Hexagon and Pyramid. *J. Phys. Chem. B* **2006**, *110*, 9448–9451.

(74) Murray, C. B.; Norris, D. J.; Bawendi, M. G. Synthesis and Characterization of Nearly Monodisperse CdE (E = S, Se, Te) Semiconductor Nanocrystallites. *J. Am. Chem. Soc.* **1993**, *115*, 8706–8715.

(75) Zhang, H.; Banfield, J. F. Identification and Growth Mechanism of ZnS Nanoparticles with Mixed Cubic and Hexagonal Stacking. *J. Phys. Chem. C* **2009**, *113*, 9681–9687.

(76) Carbone, L.; Nobile, C.; De Giorgi, M.; Sala, F. Della; Morello, G.; Pompa, P.; Hytch, M.; Snoeck, E.; Fiore, A.; Franchini, I. R.; et al. Synthesis and Micrometer-Scale Assembly of Colloidal CdSe/CdS Nanorods Prepared by a Seeded Growth Approach. *Nano Lett.* **2007**, *7*, 2942–2950.

(77) Van Huis, M. A.; Kunneman, L. T.; Overgaag, K.; Xu, Q.; Pandraud, G.; Zandbergen, H. W.; Vanmaekelbergh, D. Low-Temperature Nanocrystal Unification through Rotations and Relaxations Probed by in Situ Transmission Electron Microscopy. *Nano Lett.* **2008**, *8*, 3959–3963.

(78) Baumgardner, W. J.; Whitham, K.; Hanrath, T. Confined-but-Connected Quantum Solids via Controlled Ligand Displacement. *Nano Lett.* **2013**, *13*, 3225–3231.

(79) Hassinen, A.; Moreels, I.; De Nolf, K.; Smet, P. F.; Martins, J. C.; Hens, Z. Short-Chain Alcohols Strip X-Type Ligands and Quench the Luminescence of PbSe and CdSe

Quantum Dots, Acetonitrile Does Not. *J. Am. Chem. Soc.* **2012**, *134*, 20705–20712.

(80) Zhang, H.; Hu, B.; Sun, L.; Hovden, R.; Wise, F. W.; Muller, D. a; Robinson, R. D. Surfactant Ligand Removal and Rational Fabrication of Inorganically Connected Quantum Dots. *Nano Lett.* **2011**, *11*, 5356–5361.

(81) Wang, L. W.; Zunger, A. Local-Density-Derived Semiempirical Pseudopotentials. *Phys. Rev. B* **1995**, *51*, 17398–17416.

(82) Zhou, X. W.; Ward, D. K.; Martin, J. E.; Van Swol, F. B.; Cruz-Campa, J. L.; Zubia, D. Stillinger-Weber Potential for the II-VI Elements Zn-Cd-Hg-S-Se-Te. *Phys. Rev. B - Condens. Matter Mater. Phys.* **2013**, *88*, 1–14.

(83) Wall, M. R.; Neuhauser, D. Extraction, through Filter-Diagonalization, of General Quantum Eigenvalues or Classical Normal Mode Frequencies from a Small Number of Residues or a Short-Time Segment of a Signal. I. Theory and Application to a Quantum-Dynamics Model. *J. Chem. Phys.* **1995**, *102*, 8011–8022.

(84) Toledo, S.; Rabani, E. Verly Large Electronic Structure Calculations Using an Out-of-Core Filter-Diagonalization Method. *J. Comput. Phys.* **2002**, *180*, 256–269.

(85) Rohlfing, M.; Louie, S. G. Electron-Hole Excitations and Optical Spectra from First Principles. *Phys. Rev. B - Condens. Matter Mater. Phys.* **2000**, *62*, 4927–4944.

(86) Eshet, H.; Grünwald, M.; Rabani, E. The Electronic Structure of CdSe/CdS Core/Shell Seeded Nanorods: Type-I or Quasi-Type-II? *Nano Lett.* **2013**, *13*, 5880–5885.

(87) Ekimov, A. I.; Kudryavtsev, I. A.; Efros, A. L.; Yazeva, T. V.; Hache, F.; Schanne-Klein, M. C.; Rodina, A. V.; Ricard, D.; Flytzanis, C. Absorption and Intensity-Dependent Photoluminescence Measurements on CdSe Quantum Dots: Assignment of the First Electronic Transitions. *J. Opt. Soc. Am. B* **1993**, *10*, 100.

(88) Li, D.; Nielsen, M. H.; Lee, J. R. I.; Frandsen, C.; Banfield, J. F.; De Yoreo, J. J. Direction-Specific Interactions Control Crystal Growth by Oriented Attachment. *Science* **2012**, *336*, 1014–1018.

(89) Xin, Y.; Pennycook, S. J.; Browning, N. D.; Nellist, P. D.; Sivananthan, S.; Omnès, F.; Beaumont, B.; Faurie, J. P.; Gibart, P. Direct Observation of the Core Structures of Threading Dislocations in GaN. *Appl. Phys. Lett.* **1998**, *72*, 2680–2682.

(90) Drum, C. M. Intersecting Faults on Basal and Prismatic Planes in Aluminium Nitride. *Philos. Mag.* **1965**, *11*, 313–334.

(91) Zakharov, D. N.; Liliental-Weber, Z.; Wagner, B.; Reitmeier, Z. J.; Preble, E. A.; Davis, R. F. Structural TEM Study of Nonpolar A-Plane Gallium Nitride Grown on (11$\bar{2}$0)4H-SiC by Organometallic Vapor Phase Epitaxy. *Phys. Rev. B - Condens. Matter Mater. Phys.* **2005**, *71*, 1–9.

(92) Ruterana, P.; Barbaray, B.; Béré, A.; Vermaut, P.; Hairie, A.; Paumier, E.; Nouet, G.; Salvador, A.; Botchkarev, A.; Morkoç, H. Formation Mechanism and Relative Stability of the {1120} Stacking Fault Atomic Configurations in Wurtzite (Al,Ga,In) Nitrides. *Phys. Rev. B* **1999**, *59*, 15917–15925.

(93) Northrup, J. E. Theory of the (12_10) Prismatic Stacking Fault in GaN. *Appl. Phys. Lett.* **1998**, *72*, 2316–2318.

(94) Blank, H.; Delavignette, P.; Gevers, R.; Amelinckx, S. Fault Structures in Wurtzite. *Phys. Status Solidi* **1964**, *7*, 747–764.

(95) Fitzgerald, A. G.; Mannami, M. Electron Diffraction from Crystal Defects: Fraunhofer Effects from Plane Faults. *Proc. R. Soc. London. Ser. A. Math. Phys. Sci.* **1966**, *293*, 169–180.

(96) Hauwiller, M. R.; Ondry, J. C.; Alivisatos, A. P. Using Graphene Liquid Cell Transmission Electron Microscopy to Study in Situ Nanocrystal Etching. *J. Vis. Exp.* **2018**, *135*, 1–9.

(97) Kisielowski, C. Observing Atoms at Work by Controlling Beam-Sample Interactions. *Adv. Mater.* **2015**, *27*, 5838–5844.

(98) Van Dyck, D.; Lobato, I.; Chen, F. R.; Kisielowski, C. Do You Believe That Atoms Stay in Place When You Observe Them in HREM? *Micron* **2015**, *68*, 158–163.

(99) Anderson, P. M.; Hirth, J. P.; Lothe, J. *Theory of Dislocations Third Edition*; 2017.

(100) Kumar, A.; Subramaniam, A. Stable Edge Dislocations in Finite Crystals. *Philos. Mag.* **2012**, *92*, 2947–2956.

(101) Zheng, H.; Wang, J.; Huang, J. Y.; Wang, J.; Zhang, Z.; Mao, S. X. Dynamic Process of Phase Transition from Wurtzite to Zinc Blende Structure in InAs Nanowires. *Nano Lett.* **2013**, *13*, 6023–6027.

(102) Cortès, R.; Witz, C.; Mokili, B.; Froment, M.; Lafait, J.; Lincot, D.; Bernard, M. C. Phase Transition and Related Phenomena in Chemically Deposited Polycrystalline Cadmium Sulfide Thin Films. *J. Phys. Chem. B* **2002**, *101*, 2174–2181.

(103) Lee, S. M.; Belkhir, M. A.; Zhu, X. Y.; Lee, Y. H.; Hwang, Y. G. Electronic Structures of GaN Edge Dislocations. *Phys. Rev. B - Condens. Matter Mater. Phys.* **2000**, *61*, 16033–16039.

(104) Pu, C.; Peng, X. To Battle Surface Traps on CdSe/CdS Core/Shell Nanocrystals: Shell Isolation versus Surface Treatment. *J. Am. Chem. Soc.* **2016**, *138*, 8134–8142.

(105) Bastard, G. *Wave Mechanics Applied to Semiconductor Heterostructures*; 1991.

(106) Tadjine, A.; Delerue, C. Anderson Localization Induced by Gauge-Invariant Bond-Sign Disorder in Square PbSe Nanocrystal Lattices. *Phys. Rev. B* **2018**, *98*, 1–10.

(107) Zakharov, O.; Rubio, A.; Blase, X.; Cohen, M. L.; Louie, S. G. Quasiparticle Band Structures of Six II-VI Compounds: ZnS, ZnSe, ZnTe, CdS, CdSe, and CdTe. *Phys. Rev. B* **1994**, *50*, 10780–10787.

(108) Park, C.-H.; Louie, S. G. Making Massless Dirac Fermions from a Patterned Two-Dimensional Electron Gas. *Nano Lett.* **2009**, *9*, 1793–1797.

(109) Madelung, O. *Semiconductor Data Hand Book*; 2004.

(110) Ithurria, S.; Tessier, M. D.; Mahler, B.; Lobo, R. P. S. M.; Dubertret, B.; Efros, A. L. Colloidal Nanoplatelets with Two-Dimensional Electronic Structure. *Nat. Mater.* **2011**, *10*, 936–941.

(111) Efros, A. L.; Rosen, M. The Electronic Structure of Semiconductor Nanocrystals. *Annu. Rev. Mater. Sci.* **2000**, *30*, 475–521.

(112) Reich, K. V; Shklovskii, B. I. Exciton Transfer in Array of Epitaxially Connected Nanocrystals. *ACS Nano* **2016**, *10*, 10267–10274.

(113) Konstantatos, G.; Levina, L.; Fischer, A.; Sargent, E. H. Engineering the Temporal Response of Photoconductive Photodetectors via Selective Introduction of Surface Trap States. *Nano Lett.* **2008**, *8*, 1446–1450.

(114) Visoly-Fisher, I.; Cohen, S. R.; Ruzin, A.; Cahen, D. How Polycrystalline Devices Can Outperform Single-Crystal Ones: Thin Film CdTe/CdS Solar Cells. *Adv. Mater.* **2004**, *16*, 879–883.

(115) Boneschanscher, M. P.; Evers, W. H.; Geuchies, J. J.; Altlantzis, T.; Goris, B.; Rabouw, F. T.; van Rossum, S. A. P.; van der Zant, H. S. J.; Siebbeles, L. D. A.; Van Tendeloo, G.; et al. Long-Range Orientation and Atomic Attachment of Nanocrystals in 2D Honeycomb Superlattices. *Science* **2014**, *344*, 1377–1380.

(116) Whitham, K.; Hanrath, T. Formation of Epitaxially Connected Quantum Dot Solids: Nucleation and Coherent Phase Transition. *J. Phys. Chem. Lett.* **2017**, *8*, 2623–2628.

(117) Whitham, K.; Smilgies, D.-M.; Hanrath, T. Entropic, Enthalpic and Kinetic Aspects of Interfacial Nanocrystal Superlattice Assembly and Attachment. *Chem. Mater.* **2018**, *30*, 54–63.

(118) Jin, B.; Sushko, M. L.; Liu, Z.; Jin, C.; Tang, R. In Situ Liquid Cell TEM Reveals Bridge-Induced Contact and Fusion of Au Nanocrystals in Aqueous Solution. *Nano Lett.* **2018**, *18*, 6551–6556.

(119) Cho, K.-S.; Talapin, D. V; Gaschler, W.; Murray, C. B. Designing PbSe Nanowires and Nanorings through Oriented Attachment of Nanoparticles. *J. Am. Chem. Soc.* **2005**, *127*, 7140–7147.

(120) Koh, W.; Bartnik, A. C.; Wise, F. W.; Murray, C. B. Synthesis of Monodisperse PbSe Nanorods: A Case for Oriented Attachment. *J. Am. Chem. Soc.* **2010**, *132*, 3909–3913.

(121) van Overbeek, C.; Peters, J. L.; van Rossum, S. A. P.; Smits, M.; van Huis, M. A.; Vanmaekelbergh, D. Interfacial Self-Assembly and Oriented Attachment in the Family of PbX (X = S, Se, Te) Nanocrystals. *J. Phys. Chem. C* **2018**, *122*, 12464–12473.

(122) Peters, J. L.; Altantzis, T.; Lobato, I.; Jazi, M. A.; Overbeek, C. Van. Mono- and Multilayer Silicene-Type Honeycomb Lattices by Oriented Attachment of PbSe Nanocrystals : Synthesis , Structural Characterization , and Analysis of the Disorder . *Chem. Mater.* **2018**, *30*, 4831–4837.

(123) Wu, X. H.; Fini, P.; Tarsa, E. J.; Heying, B.; Keller, S.; Mishra, U. K.; DenBaars, S. P.; Speck, J. S. Dislocation Generation in GaN Heteroepitaxy. *J. Cryst. Growth* **1998**, *189–*

190, 231–243.

(124) Liu, X.; Li, D.; Sun, X.; Li, Z.; Song, H.; Jiang, H.; Chen, Y. Stress-Induced in Situ Epitaxial Lateral Overgrowth of High-Quality GaN. *CrystEngComm* **2014**, *16*, 8058–8063.

(125) Ning, X. J.; Chien, F. R.; Pirouz, P.; Yang, J. W.; Khan, M. A. Growth Defects in GaN Films on Sapphire: The Probable Origin of Threading Dislocations. *J. Mater. Res.* **1996**, *11*, 580–592.

(126) Potin, V.; Ruterana, P.; Nouet, G.; Pond, R. Mosaic Growth of GaN on (0001) Sapphire: A High-Resolution Electron Microscopy and Crystallographic Study of Threading Dislocations from Low-Angle to High-Angle Grain Boundaries. *Phys. Rev. B - Condens. Matter Mater. Phys.* **2000**, *61*, 5587–5599.

(127) Lee, J.; Lee, E. K.; Joo, W.; Jang, Y.; Kim, B.; Lim, J. Y.; Choi, S.; Ahn, S. J.; Ahn, J. R.; Park, M.; et al. Wafer-Scale Growth of Single-Crystal Monolayer Graphene on Reusable Hydrogen-Terminated Germanium. *Science* **2014**, *344*, 286–290.

(128) Song Lee, J.; Ho Choi, S.; Joon Yun, S.; In Kim, Y.; Boandoh, S.; Park, J.-H.; Gyu Shin, B.; Ko, H.; Hee Lee, S.; Kim, Y.-M.; et al. Wafer-Scale Single-Crystal Hexagonal Boron Nitride Film via Self-Collimated Grain Formation. *Science* **2018**, *362*, 817–821.

(129) Gomez, L.; Lin, J.; de Weerd, C.; Poirier, L.; Boehme, S. C.; von Hauff, E.; Fujiwara, Y.; Suenaga, K.; Gregorkiewicz, T. Extraordinary Interfacial Stitching between Single All-Inorganic Perovskite Nanocrystals. *ACS Appl. Mater. Interfaces* **2018**, *10*, 5984–5991.

(130) Morrell, M. V; He, X.; Luo, G.; Thind, A. S.; White, T. A.; Hachtel, A.; Borisevich, A. Y.; Idrobo, J.; Mishra, R.; Xing, Y. Significantly Enhanced Emission Stability of CsPbBr3 Nanocrystals via Chemically Induced Fusion Growth for Optoelectronic Devices via Chemically Induced Fusion Growth for Optoelectronic Devices. *ACS Appl. Nano Mater.* **2018**, *1*, 6091–6098.

(131) Thind, A. S.; Luo, G.; Hachtel, J. A.; Morrell, M. V.; Cho, S. B.; Borisevich, A. Y.; Idrobo, J.-C.; Xing, Y.; Mishra, R. Atomic Structure and Electrical Activity of Grain Boundaries and Ruddlesden-Popper Faults in Cesium Lead Bromide Perovskite. *Adv. Mater.* **2018**, *1805047*, 1805047.

(132) Thind, A. S.; Luo, G.; Hachtel, J. A.; Goriacheva, M.; Cho, S. B.; Borisevich, A.; Idrobo, J. C.; Xing, Y.; Mishra, R. Atomic-Scale Identification of Planar Defects in Cesium Lead Bromide Perovskite Nanocrystals. *Microsc. Microanal.* **2018**, *24*, 100–101.

(133) Kalesaki, E.; Evers, W. H.; Allan, G.; Vanmaekelbergh, D.; Delerue, C. Electronic Structure of Atomically Coherent Square Semiconductor Superlattices with Dimensionality below Two. *Phys. Rev. B - Condens. Matter Mater. Phys.* **2013**, *88*, 1–9.

(134) Yu, W. W.; Qu, L.; Guo, W.; Peng, X. Experimental Determination of the Extinction Coefficient of CdTe , CdSe , and CdS Nanocrystals. *Chem. Mater.* **2003**, *125*, 2854–2860.

(135) Regan, W.; Alem, N.; Alemán, B.; Geng, B.; Girit, Ç.; Maserati, L.; Wang, F.; Crommie, M.; Zettl, A. A Direct Transfer of Layer-Area Graphene. *Appl. Phys. Lett.* **2010**, *96*, 11–13.

(136) Hirel, P. Atomsk: A Tool for Manipulating and Converting Atomic Data Files. *Comput. Phys. Commun.* **2015**, *197*, 212–219.

(137) Plimpton, S. Fast Parallel Algorithms for Short-Range Molecular Dynamics. *J. Comput. Phys.* **1995**, *117*, 1–19.

(138) Rabani, E.; Hetényi, B.; Berne, B. J.; Brus, L. E. Electronic Properties of CdSe Nanocrystals in the Absence and Presence of a Dielectric Medium. *J. Chem. Phys.* **1999**, *110*, 5355–5369.

TOC Figure: